Stabilized Shock Hydrodynamics: IV. Computations with a Conservative Updated Lagrangian Method☆

G. Scovazzi[a,*], J. N. Shadid[b], E. Love[a], T. J. R. Hughes[c]

[a] *1431 Computational Shock- and Multi-physics Department, Sandia National Laboratories, P.O. Box 5800, MS 1319, Albuquerque, NM 87185-1319, USA*
[b] *1437 Electrical and Microsystem Modeling Department, Sandia National Laboratories, P.O. Box 5800, MS 0378, Albuquerque, NM 87185-0378, USA*
[c] *Institute for Computational Engineering and Sciences, The University of Texas at Austin, 1 University Station C0200, Austin, TX 78712-0027, USA*

Abstract

A new variational multiscale, stabilized method based on a piecewise linear approximation of the equations for Lagrangian shock hydrodynamics is presented. Acoustic instabilities (e.g., hourglass modes) are controlled by a stabilizing operator derived using the variational multi-scale analysis paradigm. The method is implemented using a predictor/multi-corrector time integrator which guarantees global conservation of mass, momentum, and total energy for each iterate, and represents an important advance with respect to previous work by some of the authors on the subject. Encouraging numerical comparisons with existing methods in the case of quadrilateral and hexahedral elements are presented.

Key words: Lagrangian shock hydrodynamics, stabilized methods, variational multiscale analysis, updated Lagrangian formulation, computational acoustics, hourglass control, pressure instabilities, nodal finite element method.

1. Introduction

In recent years, renewed effort has been devoted to the technical advancement of Lagrangian shock hydrodynamics algorithms (*hydrocodes* in short). A (non-exhaustive) list of recent work to advance the robustness and accuracy of hydrocodes includes [1, 2, 4–12, 20–26, 33–35]. Very recent developments [2, 6–10, 24–26] have focussed on reducing mesh distortion while maintaining second-order accuracy in smooth regions of the flow.

This article presents an implementation of the stabilization concept proposed in [32], aimed at improving the robustness and accuracy of newly developed methods for Lagrangian shock hydrodynamics on piece-wise linear, continuous approximations [31, 33]. The proposed method adopts a piece-wise linear approximation of both thermodynamic and kinematic variables, contrary to more traditional approaches in shock hydrodynamics, which rely on a piece-wise constant discretization of the thermodynamic variables. The present work stems from the earlier work in [31, 33], and represents a considerable advance from many points of view.

First of all, the proposed variational formulation of the shock hydrodynamics equations is developed using an updated Lagrangian approach, that is, the variational formulation is expressed in the current configuration (see [3] for details on this nomenclature). This strategy contrasts with the formulation in [33], which was posed in the original configuration (total or pure Lagrangian approach). The proposed updated Lagrangian approach allows for a reduction in the computational costs, as the deformation gradient does not need to be evaluated explicitly, but is implicitly accounted for when the mesh nodal coordinates are updated. In addition, algorithms for fast dynamics posed in the current configuration usually enjoy improved discrete invariance and objectivity properties relative to corresponding algorithms cast in the original configuration (see [3, 14, 38] and references therein, for more details).

Second, the proposed method adopts a second-order predictor/multi-corrector, mid-point type time integration procedure similar to [34, 35], to preserve at each iteration global mass, momentum, and total energy. This is in contrast to the predictor/multi-corrector space-time integrator proposed in [33], in which conservation is guaranteed only when convergence of the iterative process is attained. For more details on the stability and accuracy properties of the proposed predictor/multi-corrector algorithm, the reader can refer to [36].

Third, the use of lumped mass matrices in the momentum and internal energy time integration provides increased robustness under severe shock conditions. One of the problematic issues discovered in the development of the algorithm presented in [33] was that negative undershoots of the pressure and internal energy could occur in a number of challenging test cases. The combination of mass lumping with the new time-integrator

☆This research was partially funded by the DOE NNSA Advanced Scientific Computing Program and the Computer Science Research Institute at Sandia National Laboratories. Sandia is a multiprogram laboratory operated by Sandia Corporation, a Lockheed Martin Company, for the United States Department of Energy under contract DEAC04-94-AL85000.

*Corresponding author
Email addresses: gscovaz@sandia.gov (G. Scovazzi)

has eliminated this problem. This result is very important especially when complex constitutive models, usually in tabular form, are used in the computations.

The overall result is a method of improved robustness and accuracy, with very encouraging performance on a number of challenging computations, such as the three-dimensional Noh [28] and Sedov [37] tests on Cartesian (i.e, non-polar) meshes.

Although the proposed method can also be applied to triangular and tetrahedral finite element meshes (see [33], for an example in the context of earlier developments), the focus of the present paper is on computations with quadrilaterals and hexahedral elements. Focusing exclusively on these types of mesh topologies allows us to present extensive numerical comparisons with respect to earlier methods developed by some of the authors [33–35], and other research groups [1, 22]. Additional developments on triangular and tetrahedral meshes will be the object of future publications.

The rest of the exposition is organized as follows: Section 2 is devoted to presenting the equations of Lagrangian hydrodynamics and highlighting their structure as a nonlinear system of wave propagation equations. In Section 3 we present the variational form of the equations, while in Section 4 we introduce the time-integration strategy with a discussion on its conservation properties. Section 5 is dedicated to the implementation of the variational multscale stabilizing operators developed in [32], further analyzing their properties from an algorithmic point of view. In Section 6 we introduce the discontinuity capturing operators (artificial viscosities), needed to further stabilize the proposed formulation in the presence of shock waves. General considerations on the implementation and time-step control are presented in Section 7, while Section 8 is devoted to the discussion and comparison of numerical results, in two and three dimensions. A summary of conclusions is presented in Section 9.

2. Equations of Lagrangian shock hydrodynamics

The classical equations of Lagrangian shock hydrodynamics govern the rate of change in position, momentum and energy of a compressible body of fluid, as it deforms. Let Ω_0 and Ω be open sets in $\mathbb{R}^{n_d}$ (where n_d is the number of spatial dimensions). The *deformation*

$$\boldsymbol{\varphi} : \Omega_0 \to \Omega = \boldsymbol{\varphi}(\Omega_0) \,, \tag{1}$$

$$\boldsymbol{X} \mapsto \boldsymbol{x} = \boldsymbol{\varphi}(\boldsymbol{X}, t) \,, \quad \forall \boldsymbol{X} \in \Omega_0,\ t \geq 0 \,, \tag{2}$$

maps the material coordinate $\boldsymbol{X}$, representing the initial position of an infinitesimal material particle of the body, to $\boldsymbol{x}$, the position of that particle in the current configuration (see Fig. 1). Ω_0 is the domain occupied by the body in its initial configuration, with boundary Γ_0. $\boldsymbol{\varphi}$ maps Ω_0 to Ω, the domain occupied by the body in its current configuration, with boundary Γ. $\boldsymbol{\varphi}$ is usually a *smooth*, invertible map, so that the *deformation gradient*, and

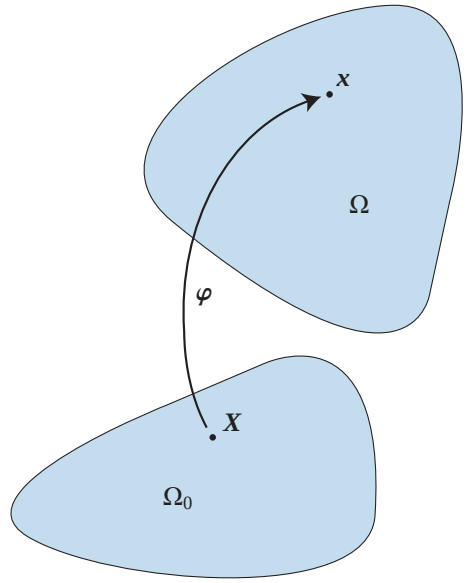

Figure 1: Sketch of the Lagrangian map $\boldsymbol{\varphi}$.

the *deformation Jacobian determinant* can be defined:

$$\boldsymbol{F} = \nabla_x \boldsymbol{\varphi} \,, \quad \text{or, in index notation,} \quad F_{iA} = \frac{\partial \varphi_i}{\partial X_A} = \frac{\partial x_i}{\partial X_A} \,, \tag{3}$$

$$J = \det(\boldsymbol{F}) \,, \tag{4}$$

where ∇_x is the gradient in the original configuration. In the domain Ω, the equations for the displacement update and conservation of mass, momentum, and energy read:

$$\dot{\boldsymbol{u}} = \boldsymbol{v} \,, \tag{5}$$

$$\rho J = \rho_0 \,, \tag{6}$$

$$\rho \dot{\boldsymbol{v}} = \rho\, \boldsymbol{b} + \nabla_x \cdot \boldsymbol{\sigma} \,, \tag{7}$$

$$\rho \dot{\epsilon} = \rho\, r + \nabla_x \boldsymbol{v} : \boldsymbol{\sigma} + \nabla_x \cdot \boldsymbol{q} \,. \tag{8}$$

Here, ∇_x and $\nabla_x \cdot$ are the current configuration gradient and divergence operators, and $\dot{(\cdot)}$ indicates the material, or Lagrangian, time derivative. $\boldsymbol{u} = \boldsymbol{x} - \boldsymbol{X}$ is the displacement vector, ρ_0 is the reference (initial) density, ρ is the (current) density, $\boldsymbol{v}$ is the velocity, $\boldsymbol{b}$ is the body force (e.g., gravity), $\boldsymbol{\sigma}$ is the symmetric Cauchy stress tensor, r is the energy source term, and $\boldsymbol{q}$ is the heat flux. We also denote by $E = \epsilon + \boldsymbol{v} \cdot \boldsymbol{v}/2$ the total energy, the sum of the internal energy ϵ and the kinetic energy $\boldsymbol{v} \cdot \boldsymbol{v}/2$. E, ϵ, $\boldsymbol{b}$, r are measured per unit mass. Equations (5)–(8) are most commonly adopted in shock-hydrodynamics algorithms [5], and make use of the quasi-linear rather than the conservative form of the internal energy equation. The sum of the internal energy equation (8) and the kinetic energy equation (the scalar product of (7) with the velocity vector $\boldsymbol{v}$) yields the equation for the conservation of total energy.

Remark1. Although (8) is not in conservative form, it can still be used to develop a globally conservative variational formulation, as will be shown in Section 4.

Assuming that the boundary $\Gamma = \partial\Omega$ is partitioned as $\Gamma = \overline{\Gamma^g \cup \Gamma^h}$, $\Gamma^g \cap \Gamma^h = \emptyset$, *displacement boundary conditions* are

enforced on the *Dirichlet* boundary Γ^g, that is,

$$\boldsymbol{u}|_{\Gamma^g} = \boldsymbol{u}_{bc}(\boldsymbol{x}, t) \ , \tag{9}$$

and *traction boundary conditions* are enforced on the *Neumann* boundary Γ^h, by means of a physical traction vector $\boldsymbol{t}$, that is,

$$\boldsymbol{\sigma}\boldsymbol{n}|_{\Gamma^h} = \boldsymbol{t}(\boldsymbol{x}, t) \ . \tag{10}$$

Equations (5)–(8), and boundary conditions (9)-(10) completely define the evolution of the system, once appropriate initial conditions are specified.

2.1. Constitutive laws

The analysis presented in what follows is specific to materials with no deformation strength. In this case, the Cauchy stress $\boldsymbol{\sigma}$ reduces to an isotropic tensor, dependent only on the thermodynamic pressure:

$$\boldsymbol{\sigma} \ = \ -p\boldsymbol{I}_{n_d \times n_d} \ , \tag{11}$$

An equation of state of the type

$$p = \hat{p}(\rho, \epsilon) \ , \tag{12}$$

is assumed. For example, equations of state of Mie-Grüneisen type are compatible with (12), namely

$$\hat{p}(\rho, \epsilon) \ = \ f_1(\rho) + f_2(\rho)\epsilon \ , \tag{13}$$

and apply to materials such as compressible ideal gases, co-volume gases, high explosives, etc. (See [27] for more details.) Ideal gases satisfy (13), with $f_1 = 0$ and $f_2 = (\gamma - 1)\rho$, to yield

$$\hat{p}(\rho, \epsilon) = (\gamma - 1)\rho\epsilon \ . \tag{14}$$

3. Variational formulation

The first step in the development of a variational form for (5)–(8) is to define the *trial* spaces for the kinematic and thermodynamic variables, characterizing the *state* of the system. Let $\mathcal{S}_\kappa$ denote the space of admissible values for the kinematic variables (displacements, velocities, accelerations), and $\mathcal{S}_\gamma$ the space of admissible thermodynamic states (densities, pressures, internal energies). In addition, *test* spaces can be defined: $\mathcal{V}_\kappa$ is the space of variations (compatible with the boundary condition (9)) for the kinematic variables, and $\mathcal{V}_\gamma$ is the space of variations for the thermodynamic variables. The complete variational problem reads:

Find $\rho, p, \epsilon \in \mathcal{S}_\gamma$, $\boldsymbol{u}, \boldsymbol{v} \in \mathcal{S}_\kappa$, *such that,* $\forall \psi \in \mathcal{V}_\gamma$, $\forall \boldsymbol{\psi} \in \mathcal{V}_\kappa$,

$$0 = \int_{\Omega_0} \boldsymbol{\psi} \cdot (\dot{\boldsymbol{u}} - \boldsymbol{v}) \ \mathrm{d}\Omega_0 \ , \tag{15}$$

$$0 = \int_{\Omega_0} \psi \, (\rho_0 - \rho J) \ \mathrm{d}\Omega_0 \ , \tag{16}$$

$$\begin{aligned} 0 = & \int_{\Omega_0} \boldsymbol{\psi} \cdot (\rho_0 \dot{\boldsymbol{v}}) \ \mathrm{d}\Omega_0 + \int_{\Omega} \nabla_x^s \boldsymbol{\psi} : \tilde{\boldsymbol{\sigma}} \ \mathrm{d}\Omega \\ & - \int_{\Gamma^h} \boldsymbol{\psi} \cdot \boldsymbol{t} \ \mathrm{d}\Gamma - \int_{\Omega} \boldsymbol{\psi} \cdot (\rho \boldsymbol{b}) \ \mathrm{d}\Omega \ , \end{aligned} \tag{17}$$

$$\begin{aligned} 0 = & \int_{\Omega_0} \psi \, (\rho_0 \dot{\epsilon}) \ \mathrm{d}\Omega_0 - \int_{\Omega} \psi \ (\nabla_x^s \boldsymbol{v} : \tilde{\boldsymbol{\sigma}} + \rho r) \ \mathrm{d}\Omega \\ & + \int_{\Omega} \nabla_x \psi \cdot \tilde{\boldsymbol{q}} \ \mathrm{d}\Omega \ , \end{aligned} \tag{18}$$

where $\nabla_x^s = 1/2(\nabla_x^T + \nabla_x)$ is the symmetric part of the gradient operator. In (17)–(18), we have used the identity $\rho_0 \, \mathrm{d}\Omega_0 = \rho \, \mathrm{d}\Omega$, which states that the mass of an infinitesimal particle $dm = \rho_0 \, \mathrm{d}\Omega_0$ does not change under the Lagrangian deformation map. The term $\tilde{\boldsymbol{\sigma}}$ denotes in general a symmetric algorithmic stress tensor, namely

$$\tilde{\boldsymbol{\sigma}} = -p\boldsymbol{I} + \boldsymbol{\sigma}_{vms} + \boldsymbol{\sigma}_{art} \ , \tag{19}$$

where $\boldsymbol{\sigma}_{vms}$ is a variational multiscale stabilizing stress tensor, and $\boldsymbol{\sigma}_{art}$ is an artificial viscosity stress tensor, designed to capture shock layers. Since $\boldsymbol{\sigma}$ is symmetric, $\nabla_x \boldsymbol{v} : \boldsymbol{\sigma} = \nabla_x^s \boldsymbol{v} : \boldsymbol{\sigma}$. Analogously, $\tilde{\boldsymbol{q}}$ denotes an algorithmic flux vector,

$$\tilde{\boldsymbol{q}} = \boldsymbol{q} + \boldsymbol{\lambda}_{vms} + \boldsymbol{\lambda}_{art} \ , \tag{20}$$

where $\boldsymbol{\lambda}_{art}$ is an artificial, shock-capturing vector flux, and $\boldsymbol{\lambda}_{vms}$ is a variational multiscale stabilizing vector flux. Both $\boldsymbol{\sigma}_{vms}$ and $\boldsymbol{\lambda}_{vms}$ are residual-based quantities. Specific derivations and definitions for the terms $\tilde{\boldsymbol{\sigma}}$ and $\tilde{\boldsymbol{q}}$ will be given in subsequent sections.

Remark2. For reasons that will become clear subsequently (see Section 5 and Section 6), $\boldsymbol{\lambda}_{vms}$ and $\boldsymbol{\lambda}_{art}$ *do not* possess the structure of heat fluxes, and this terminology is therefore inappropriate.

In the proposed spatial approximation, *all* variables (both kinematic and thermodynamic) can be approximated by piecewise linear, continuous functions (node-centered degrees-of-freedom). Consequently, the test-spaces for the equations consist of piece-wise linear, continuous functions. More precisely:

$$\begin{aligned} \mathcal{S}_\kappa^h = & \Big\{ \boldsymbol{\psi}^h \in (C^0(\Omega))^{n_d} : \boldsymbol{\psi}^h\big|_{\Omega_e} \in (\mathcal{P}_1(\Omega_e))^{n_d}, \\ & \boldsymbol{\psi}^h = \boldsymbol{g}_{bc}(t) \text{ on } \Gamma^g \Big\} \ , \end{aligned} \tag{21}$$

$$\begin{aligned} \mathcal{V}_\kappa^h = & \Big\{ \boldsymbol{\psi}^h \in (C^0(\Omega))^{n_d} : \boldsymbol{\psi}^h\big|_{\Omega_e} \in (\mathcal{P}_1(\Omega_e))^{n_d}, \\ & \boldsymbol{\psi}^h = \boldsymbol{0} \text{ on } \Gamma^g \Big\} \ , \end{aligned} \tag{22}$$

$$\mathcal{S}_\gamma^h = \Big\{ \psi^h \in C^0(\Omega) : \psi^h\big|_{\Omega_e} \in \mathcal{P}_1(\Omega_e), \Big\} \ , \tag{23}$$

$$\mathcal{V}_\gamma^h = \mathcal{S}_\gamma^h \ , \tag{24}$$

where $\mathcal{P}_1(\Omega_e)$ is the space of piece-wise linear polynomials over the element e, and $\boldsymbol{g}_{bc}(t)$ indicates the generalized essential (Dirichlet) boundary conditions, possibly dependent on time. For example, if $\mathcal{S}^h_\kappa$ is used to approximate displacements, then $\boldsymbol{g}_{bc} = \boldsymbol{u}_{bc}$. If instead $\mathcal{S}^h_\kappa$ is used to approximate velocities, then $\boldsymbol{g}_{bc}$ indicates a boundary velocity $\boldsymbol{v}_{bc}$, compatible with $\boldsymbol{u}_{bc}$.

Remark3. In the current formulation, traction (i.e., *natural*) boundary conditions are imposed in (17) through the weak form, while the space $\mathcal{S}_\kappa$ incorporates the set of *essential* boundary conditions (9). Consequently, boundary conditions of kinematic (Dirichlet) type are imposed *strongly*.

Remark4. In contrast with previous work in [33], the density is also expressed with piece-wise linear continuous functions. Numerical results not be reported here, for the sake of brevity, showed little difference between the two approaches.

4. Time integration and discrete weak forms

The variational form of the Lagrangian hydrodynamics equations and its conservation properties are strictly related to the choice of time-integration algorithm. In the present work, an explicit iterative time integrator is derived by combining a mid-point method with a predictor/multi-corrector strategy. The proposed formulation conserves mass, momentum and total energy without resorting to any staggered approach in time, and stems from previous work in [35] (and also from similar ideas developed in the context of *mimetic* or *compatible* discretizations [2, 10]).

4.1. Discrete equations

For the sake of simplicity, it is assumed that the body force $\boldsymbol{b}$, the heat flux $\boldsymbol{q}$ and the heat source/sink r are absent. The time step is indicated by Δt, and the mid-point value of a quantity f is defined as:

$$f_{n+1/2} = \frac{f_n + f_{n+1}}{2} \,, \tag{25}$$

where $f_n = f(t_n)$. In what follows, with slight abuse of notation, the superscript "h" - denoting numerical discretization - is omitted from the solution variables, discrete gradient operators, and the domain geometry.

4.1.1. Momentum balance

The variational problem associated with the conservation of linear momentum reads

Find $\boldsymbol{v} \in \mathcal{S}^h_\kappa$, *such that,* $\forall \boldsymbol{\psi}^h \in \mathcal{V}^h_\kappa$,

$$\begin{aligned} 0 = &\int_{\Omega_0} \boldsymbol{\psi}^h \cdot \rho_0 \left(\boldsymbol{v}_{n+1} - \boldsymbol{v}_n\right) \, \mathrm{d}\Omega_0 \\ &+ \Delta t \int_{\Omega_{n+1/2}} (\nabla_x \boldsymbol{\psi}^h)_{n+1/2} : \tilde{\boldsymbol{\sigma}}_{n+1/2} \, \mathrm{d}\Omega \\ &- \Delta t \int_{\Gamma^h_{n+1/2}} \boldsymbol{\psi}^h \cdot \boldsymbol{t}_{n+1/2} \, \mathrm{d}\Gamma \,, \end{aligned} \tag{26}$$

where the physical traction $\boldsymbol{t}$ acts only on the Neumann boundary (i.e., $\boldsymbol{t}|_{\Gamma^g} = 0$). The variational form (26) yields the following discrete equations, for the nodal vector $\mathbf{v}$ of velocity degrees-of-freedom:

$$[\mathbf{M}_v] \left(\mathbf{v}_{n+1} - \mathbf{v}_n\right) + \Delta t \, \mathbf{F}_{n+1/2} = \mathbf{0} \,, \tag{27}$$

where mass lumping has been applied to

$$[\mathbf{M}_v] = [\mathrm{diag}(\mathbf{M}_0, \mathbf{M}_0, \mathbf{M}_0)] \,, \tag{28}$$

a diagonal $[(n_d \times n_{np}) \times (n_d \times n_{np})]$-matrix ($n_{np}$ is the number of nodes in the mesh). Specifically, using N_A to indicate the shape function associated with node A in the global node numbering, the vector $\mathbf{M}_0$ is defined as

$$\mathbf{M}_0 = \{\mathsf{M}_{0;A}\} \,, \tag{29}$$

$$\mathsf{M}_{0;A} = \int_{\Omega_0} N_A \rho_0 \, \mathrm{d}\Omega_0 \,. \tag{30}$$

Analogously, $\mathbf{F}_{n+1/2}$ is a $(n_d \times n_{np})$-vector:

$$\mathbf{F}_{n+1/2} = \{\mathbf{F}_{n+1/2;A}\} \,, \tag{31}$$

$$\begin{aligned} \mathbf{F}_{n+1/2;A} = &\int_{\Omega_{n+1/2}} \tilde{\boldsymbol{\sigma}}_{n+1/2} (\nabla_x N_A)_{n+1/2} \, \mathrm{d}\Omega \\ &- \int_{\Gamma_{n+1/2}} N_A \boldsymbol{t}_{n+1/2} \, \mathrm{d}\Gamma \,, \end{aligned} \tag{32}$$

4.1.2. Energy balance

Discretizing (18) in time yields:

Find $\epsilon \in \mathcal{S}^h_\gamma$, *such that,* $\forall \psi^h \in \mathcal{V}^h_\gamma$,

$$\begin{aligned} 0 = &\int_{\Omega_0} \psi^h \rho_0 \left(\epsilon_{n+1} - \epsilon_n\right) \, \mathrm{d}\Omega_0 \\ &- \Delta t \int_{\Omega_{n+1/2}} \psi^h \, (\nabla_x \boldsymbol{v})_{n+1/2} : \tilde{\boldsymbol{\sigma}}_{n+1/2} \, \mathrm{d}\Omega \\ &- \int_{\Omega_{n+1/2}} \nabla_x \psi^h \cdot \tilde{\boldsymbol{q}}_{n+1/2} \, \mathrm{d}\Omega \,, \end{aligned} \tag{33}$$

so that an update equation for the nodal vector $\boldsymbol{\epsilon}$ of internal energy degrees-of-freedom can be derived:

$$[\mathbf{M}_\epsilon] \left(\boldsymbol{\epsilon}_{n+1} - \boldsymbol{\epsilon}_n\right) + \Delta t \, \mathbf{W}_{n+1/2} = \mathbf{0} \,, \tag{34}$$

where $[\mathbf{M}_\epsilon] = [\mathrm{diag}(\mathbf{M}_0)]$, and $\mathbf{W}_{n+1/2}$ is a n_{np}-dimensional vector defined as

$$\mathbf{W}_{n+1/2} = \{\mathsf{W}_{n+1/2;A}\} \,, \tag{35}$$

$$\begin{aligned} \mathsf{W}_{n+1/2;A} = &- \int_{\Omega_{n+1/2}} N_A \, (\nabla_x \boldsymbol{v})_{n+1/2} : \tilde{\boldsymbol{\sigma}}_{n+1/2} \, \mathrm{d}\Omega \\ &+ \int_{\Omega_{n+1/2}} (\nabla_x N_A) \cdot \tilde{\boldsymbol{q}}_{n+1/2} \, \mathrm{d}\Omega \,. \end{aligned} \tag{36}$$

4.1.3. Mass balance

The mass conservation equation (16) can be slightly rearranged to yield:

Find $\rho \in \mathcal{S}^h_\gamma$*, such that,* $\forall \psi^h \in \mathcal{V}^h_\gamma$*,*

$$\int_{\Omega_0} \psi^h \rho_0 \, \mathrm{d}\Omega_0 = \int_{\Omega_0} \psi^h \rho J \, \mathrm{d}\Omega_0 = \int_{\Omega} \psi^h \rho \, \mathrm{d}\Omega \ . \tag{37}$$

Testing the previous equation using nodal shape functions yields

$$[\mathbf{V}_{n+1}]\boldsymbol{\rho}_{n+1} = \mathbf{M}_0 \ , \tag{38}$$

where $\boldsymbol{\rho}_{n+1}$ is the vector of nodal degrees-of-freedom for the density at t_{n+1}, that is,

$$\boldsymbol{\rho}_{n+1} = \{\rho_{n+1;A}\} \ , \tag{39}$$

and $[\mathbf{V}_{n+1}] = [\mathrm{diag}(\mathbf{V}_{n+1})]$ is the diagonal matrix of (lumped) nodal volumes, with

$$\mathbf{V}_{n+1} = \{\mathsf{V}_{n+1;A}\} \ , \tag{40}$$

$$\mathsf{V}_{n+1;A} = \int_{\Omega_0} N_A J_{n+1} \, \mathrm{d}\Omega_0 = \int_{\Omega_{n+1}} N_A \, \mathrm{d}\Omega \ . \tag{41}$$

Remark5. Following the finite-volume method nomenclature, the interpretation of $\{\mathbf{V}_{n+1}\}$ is analogous to a vector of co-volumes.

4.1.4. Displacement equations

Positions are updated from velocities using a weak projection, rather than using a set of ordinary differential equations for the nodal positions. The time-discretization of the rate equations for the position yields:

Find $\boldsymbol{u} \in \mathcal{S}^h_\gamma$*, such that,* $\forall \boldsymbol{\psi}^h \in \mathcal{V}^h_\gamma$*,*

$$\int_{\Omega_0} \boldsymbol{\psi}^h \cdot (\boldsymbol{u}_{n+1} - \boldsymbol{u}_n) \, \mathrm{d}\Omega_0 - \Delta t \int_{\Omega_0} \boldsymbol{\psi}^h \cdot \boldsymbol{v}_{n+1/2} \, \mathrm{d}\Omega_0 = 0 \tag{42}$$

and leads to the update equation for the vector $\mathbf{u}$ of nodal displacements:

$$\mathbf{u}_{n+1} - \mathbf{u}_n - \Delta t \, \mathbf{v}_{n+1/2} = \mathbf{0} \ , \tag{43}$$

with

$$\mathbf{v}_{n+1/2} = \{\mathbf{v}_{n+1/2;A}\} \ , \tag{44}$$

$$\mathbf{v}_{n+1/2;A} = \mathsf{V}^{-1}_{0;A} \left(\int_{\Omega_0} N_A \mathbf{v}_{n+1/2} \, \mathrm{d}\Omega_0 \right) \ . \tag{45}$$

Remark6. In the case of the displacement update, the inverse of a lumped volume matrix is premultiplied by the vector of nodal positions, and the velocities are tested against the nodal shape functions. This leads to an explicit procedure which is very similar in structure to the momentum equation update. This choice was preferred in [33] to the simpler approach of integrating in time ordinary differential equations for the nodal displacements, due to its superior results.

Remark7. Note also that an early attempt to apply the proposed displacement update to the more traditional finite element method in [35] (i.e., with thermodynamic variables *constant* on element interiors) proved disastrous. In fact, a number of basic tests performed with this combination could not be run to completion due to inversion of some of the element volumes. This fact seems to indicate that the proposed displacement update is effective *only* in the context of piece-wise linear approximation of thermodynamic variables.

4.1.5. Equation of state

The equation of state is evaluated at each time step at the nodal points, and a nodal pressure is computed as a function of nodal internal energy and nodal density:

$$\boldsymbol{\sigma}_{n+1} = -p_{n+1}\boldsymbol{I} = -\hat{p}(\rho_{n+1}, \epsilon_{n+1})\boldsymbol{I} \ . \tag{46}$$

A piece-wise continuous pressure field is then interpolated from the nodal values of the pressure. Therefore, we can write a discrete form of the pressure degrees-of-freedom update equation as follows:

$$\mathbf{p}_{n+1} = \hat{p}(\boldsymbol{\rho}_{n+1}, \boldsymbol{\epsilon}_{n+1}) \ . \tag{47}$$

4.2. Global conservation properties

4.2.1. Conservation of mass

Equation (38) (or, correspondingly, (37)) is a statement of global conservation of mass. This can be easily seen by testing (37) against a constant unit test function, which yields

$$\int_{\Omega_0} \rho_0 \, \mathrm{d}\Omega_0 = \int_{\Omega} \rho \, \mathrm{d}\Omega \ = \ \text{total mass} \ . \tag{48}$$

In the context of the discrete equations (with lumping applied to the second integral above), we can easily see that (48) is equivalent to contracting (38) with the vector $\mathbf{1}$, a n_{np}-dimensional vector whose entries are all unity, namely

$$\mathbf{1}^T[\mathbf{V}_{n+1}]\boldsymbol{\rho}_{n+1} = \mathbf{1}^T\{\mathbf{M}_0\} \ = \ \text{discrete total mass} \ . \tag{49}$$

4.2.2. Conservation of linear and angular momentum

Let us assume, as is customary when proving conservation statements, that only homogenous Neumann (zero-traction) boundary conditions are imposed, so that the test and trial function spaces for the velocities coincide (i.e., $\mathcal{S}^h_\kappa = \mathcal{V}^h_\kappa$). Testing (26) against the shape function $\boldsymbol{\psi}^h = \boldsymbol{e}_i$, $i = 1, \ldots, n_d$ (the *constant* unit vector of the Cartesian basis in the ith direction) yields a conservation statement for the global momentum in the direction $\boldsymbol{e}_i$. Namely, as the boundary term and the integral involving the test function gradient disappear, (26) yields

$$\begin{aligned} 0 &= \int_{\Omega_0} \rho_0 \left(v_{i,n+1} - v_{i,n}\right) \, \mathrm{d}\Omega_0 \\ &= \int_{\Omega_{n+1}} \rho_{n+1} v_{i,n+1} \, \mathrm{d}\Omega - \int_{\Omega_n} \rho_n v_{i,n} \, \mathrm{d}\Omega \ , \end{aligned} \tag{50}$$

where $v_i = \boldsymbol{v} \cdot \boldsymbol{e}_i$. This is analogous to contracting the entries of vector equation (27) corresponding to the ith component against the vector $\mathbf{1}$:

$$\mathbf{1}^T([\mathbf{M}_{i,v}]\,(\mathbf{v}_{i,n+1} - \mathbf{v}_{i,n})) = \mathbf{0} \ , \tag{51}$$

where $[\mathbf{M}_{i,v}]$ is the diagonal block of $[\mathbf{M}_v]$ corresponding to the degrees-of-freedom $\mathbf{v}_i$ associated with the ith direction. Under appropriate boundary conditions, an algorithmic form of the total angular momentum is also conserved (see [19] for a detailed discussion).

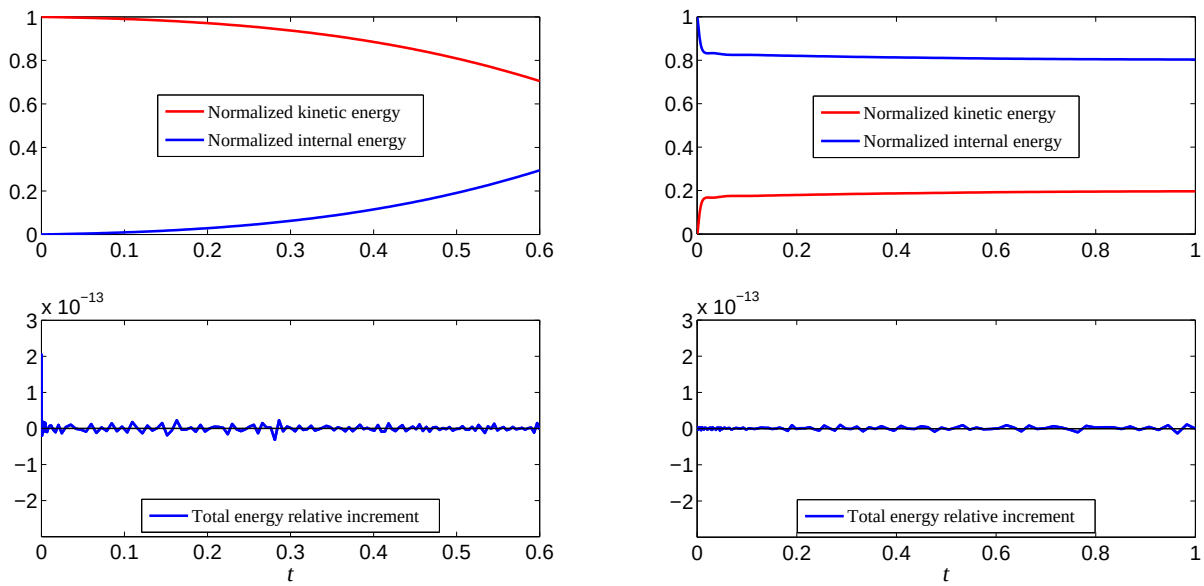

(a) Three-dimensional Noh test (30^3-element mesh).

(b) Three-dimensional Sedov test (44^3 element mesh).

Figure 2: Energy history for a three-dimensional Noh test (2(a)), and a three-dimensional Sedov test (2(b)). The plots on the upper row show the change in the internal (blue line) and kinetic (red line) energies, normalized with the total energy. The plots on the lower row show the total energy relative increment between time t_n, and t_{n+1}, namely $(\mathcal{E}^{tot}_{n+1} - \mathcal{E}^{tot}_n)/\mathcal{E}^{tot}_n$. Note the scale of the vertical axis is 10^{-13} in the lower plots.

4.2.3. Conservation of total energy

Proving conservation of total energy is somewhat less obvious. The proof will be given in the special case when mass lumping is used, although it holds also when a consistent mass matrix is used (see [32, 34, 35] for complete details). We will assume again homogenous Neumann boundary conditions, for which it is possible to test (27) with $\boldsymbol{\psi}^h = \boldsymbol{v}_{n+1/2}$. Summing over all the nodes, the kinetic energy balance for the system is obtained:

$$\frac{1}{2}\mathbf{v}^T_{n+1}[\mathbf{M}_v]\mathbf{v}_{n+1} - \frac{1}{2}\mathbf{v}^T_n[\mathbf{M}_v]\mathbf{v}_n = -\Delta t\, \mathbf{v}^T_{n+1/2}\mathbf{F}_{n+1/2} \,. \tag{52}$$

This result holds by virtue of the following identity (recall $[\mathbf{M}_v]$ is diagonal, therefore symmetric):

$$\begin{aligned}\frac{1}{2}\mathbf{v}^T_{n+1/2}[\mathbf{M}_v]\left(\mathbf{v}_{n+1} - \mathbf{v}_n\right) &= \frac{1}{2}\left(\mathbf{v}^T_{n+1} + \mathbf{v}^T_n\right)[\mathbf{M}_v]\left(\mathbf{v}_{n+1} - \mathbf{v}_n\right)\\ &= \frac{1}{2}\mathbf{v}^T_{n+1}[\mathbf{M}_v]\mathbf{v}_{n+1} - \frac{1}{2}\mathbf{v}^T_n[\mathbf{M}_v]\mathbf{v}_n \,.\end{aligned} \tag{53}$$

Testing (33) with a unit constant shape function over the entire domain (i.e., $\psi^h\big|_{\Omega_0} = 1$), is equivalent to contracting (34) with $\mathbf{1}$:

$$\mathbf{1}^T[\mathbf{M}_0]\left(\boldsymbol{\epsilon}_{n+1} - \boldsymbol{\epsilon}_n\right) = -\Delta t\, \mathbf{1}^T\mathbf{W}_{n+1/2} \,, \tag{54}$$

where, in particular, recalling $\sum_{A=1}^{n_{np}} N_A = 1$,

$$\begin{aligned}\mathbf{1}^T\mathbf{W}_{n+1/2} &= -\,\mathbf{1}^T\left\{-\int_{\Omega_{n+1/2}} N_A\,(\nabla_x \boldsymbol{v})_{n+1/2} : \tilde{\boldsymbol{\sigma}}_{n+1/2}\,\mathrm{d}\Omega\right\}\\ &\quad + \mathbf{1}^T\left\{\int_{\Omega_{n+1/2}} (\nabla_x N_A)\cdot\tilde{\boldsymbol{q}}_{n+1/2}\,\mathrm{d}\Omega\right\}\\ &= -\int_{\Omega_{n+1/2}}\left(\sum_{A=1}^{n_{np}} N_A\right)(\nabla_x \boldsymbol{v})_{n+1/2} : \tilde{\boldsymbol{\sigma}}_{n+1/2}\,\mathrm{d}\Omega\\ &\quad + \int_{\Omega_{n+1/2}} \nabla_x\left(\sum_{A=1}^{n_{np}} N_A\right)\cdot\tilde{\boldsymbol{q}}_{n+1/2}\,\mathrm{d}\Omega\\ &= -\int_{\Omega_{n+1/2}} (\nabla_x \boldsymbol{v})_{n+1/2} : \tilde{\boldsymbol{\sigma}}_{n+1/2}\,\mathrm{d}\Omega\\ &\quad + \int_{\Omega_{n+1/2}} \nabla_x(1)\cdot\tilde{\boldsymbol{q}}_{n+1/2}\,\mathrm{d}\Omega\\ &= -\int_{\Omega_{n+1/2}} (\nabla_x \boldsymbol{v})_{n+1/2} : \tilde{\boldsymbol{\sigma}}_{n+1/2}\,\mathrm{d}\Omega \,.\end{aligned} \tag{55}$$

Comparing (31)–(32) with (35)–(36), and taking into account (55),

$$\mathbf{v}^T_{n+1/2}\mathbf{F}_{n+1/2} = -\mathbf{1}^T\mathbf{W}_{n+1/2} \,. \tag{56}$$

Summing (52) and (54), we derive a statement of conservation of the algorithmic total energy:

$$\frac{1}{2}\mathbf{v}^T_{n+1}[\mathbf{M}_v]\mathbf{v}_{n+1} + \mathbf{1}^T[\mathbf{M}_0]\boldsymbol{\epsilon}_{n+1} = \frac{1}{2}\mathbf{v}^T_n[\mathbf{M}_v]\mathbf{v}_n + \mathbf{1}^T[\mathbf{M}_0]\boldsymbol{\epsilon}_n \,. \tag{57}$$

Table 1: Outline of the predictor/multi-corrector algorithm. Note that, because of mass lumping, all matrices are diagonal, so that all inverse operations are just vector divisions. Three iterations were typically used in the computations.

Retrieve loop parameters: n_{step}, $i_{\max}$
Initialize all variables with initial conditions
Form $\mathbf{M}_0$, $[\mathbf{M}_v]$, and $[\mathbf{M}_\epsilon]$
For $n = 0, \ldots, n_{\text{step}}$ (*Time-step loop begins*)
  Set Δt (respecting the CFL condition)
  Predictor: $\mathbf{Y}^{(0)}_{n+1} = \mathbf{Y}_n$
  For $i = 0, \ldots, i_{\max} - 1$ (*Multi-corrector loop begins*)
    Assembly: $\mathbf{F}^{(i)}_{n+1/2}$
    Velocity update: $\mathbf{v}^{(i+1)}_{n+1} = \mathbf{v}_n - \Delta t [\mathbf{M}_v]^{-1} \mathbf{F}^{(i)}_{n+1/2}$
    Assembly: $\mathbf{W}^{(i,i+1)}_{n+1/2}$
    Internal energy update: $\boldsymbol{\epsilon}^{(i+1)}_{n+1} = \boldsymbol{\epsilon}_n - \Delta t\, [\mathbf{M}_\epsilon]^{-1} \mathbf{W}^{(i,i+1)}_{n+1/2}$
    Position update: $\mathbf{u}^{(i+1)}_{n+1} = \mathbf{u}_n + \Delta t\, \mathbf{v}^{(i+1)}_{n+1/2}$
    Volume update: $\mathbf{V}^{(i+1)}_{n+1} = \mathbf{V}\left(\mathbf{u}^{(i+1)}_{n+1}\right)$
    Density update: $\boldsymbol{\rho}^{(i+1)}_{n+1} = [\mathbf{V}^{(i+1)}_{n+1}]^{-1} \mathbf{M}_0$
    Equation of state update: $\mathbf{p}^{(i+1)}_{n+1} = \hat{p}\left(\boldsymbol{\rho}^{(i+1)}_{n+1}, \boldsymbol{\epsilon}^{(i+1)}_{n+1}\right)$
  End *(Multi-corrector loop ends)*
  Time update: $\mathbf{Y}_{n+1} = \mathbf{Y}^{(i_{\max})}_{n+1}$
End *(Time-step loop ends)*
Exit

Remark8. The approach followed in the proof of global conservation properties, is very similar to the one presented in [35], with the exception of the treatment of the term containing $\tilde{\boldsymbol{q}}$.

4.3. A predictor/multi-corrector approach

The algorithm developed in Section 3 requires the inversion of a matrix: The force and work terms are computed at the mid-point in time, and necessitate knowledge of the solution at time t_{n+1}. However, a fully explicit procedure can be recovered by resorting to a predictor/multi-corrector approach. For this purpose, a number of preliminary definitions are needed. The state of the system at time $t = t_\bullet$ is defined by means of the vector $\mathbf{Y}_\bullet = [\mathbf{u}^T_\bullet, \mathbf{v}^T_\bullet, \boldsymbol{\rho}^T_\bullet, \boldsymbol{\epsilon}^T_\bullet, \mathbf{p}^T_\bullet]^T$. As can be appreciated in Table 1, the proposed approach consists of a velocity update, followed, in the order, by internal energy, position, density and pressure (or, more generally, stress) updates. $\mathbf{F}^{(i)}_{n+1/2}$ indicates the evaluation of $\mathbf{F}_{n+1/2}$ using the state $\mathbf{Y}$ at iterate (i). The definition of the iterate of the work vector $\mathbf{W}_{n+1/2}$ is somewhat different:

$$\mathbf{W}^{(i,j)}_{n+1/2} = \{\mathrm{W}^{(i,j)}_{n+1/2;A}\}\,, \tag{58}$$

$$\mathrm{W}^{(i,j)}_{n+1/2;A} = -\int_{\Omega^{(i)}_{n+1/2}} N_A\, ((\nabla_x)^{(i)}_{n+1/2} \mathbf{v}^{(j)}_{n+1/2}) : \tilde{\boldsymbol{\sigma}}^{(i)}_{n+1/2}\, \mathrm{d}\Omega + \int_{\Omega^{(i)}_{n+1/2}} \left(\nabla_{x^{(i)}_{n+1/2}} N_A\right) \cdot \tilde{\boldsymbol{q}}^{(i)}_{n+1/2}\, \mathrm{d}\Omega\,. \tag{59}$$

Here $\nabla_{x^{(i)}_{n+1/2}}$ and $\boldsymbol{v}^{(j)}_{n+1/2}$ indicate the (current configuration) gradient operator and the velocity field at $t = t_{n+1/2}$ and iterate i and j, respectively. This notation is needed to understand how conservation is enforced *at each iteration* of the predictor/multi-corrector procedure.

4.3.1. Algorithmic conservation of global total energy

The proposed predictor/multi-corrector approach maintains all the conservation properties of the base mid-point algorithm. Note that the work vector $\mathbf{W}^{(i,i+1)}_{n+1/2}$ (see Table 1) is computed holding the geometry and all the terms in the integral (59) at iterate (i), while the velocity $\boldsymbol{v}_{n+1/2}$ is evaluated using iterate (i+1). This new iterate is readily available after the momentum equation is integrated in time (the predictor/multi-corrector mimics a Gauss-Seidel solution strategy). Using arguments virtually identical to the ones presented in Section 4.2, it is easy to realize that the identity

$$(\mathbf{v}^{(i+1)}_{n+1/2})^T \mathbf{F}^i_{n+1/2} = -\mathbf{1}^T \mathbf{W}^{(i,i+1)}_{n+1/2} \tag{60}$$

guarantees that total energy is conserved at *each iterate* of the predictor/multi-corrector algorithm, namely,

$$\frac{1}{2}(\mathbf{v}^{(i+1)}_{n+1})^T [\mathbf{M}_v] \mathbf{v}^{(i+1)}_{n+1} + [\mathbf{M}_0] \boldsymbol{\epsilon}^{(i+1)}_{n+1} = \frac{1}{2} \mathbf{v}^T_n [\mathbf{M}_v] \mathbf{v}_n + \mathbf{M}^T_0 \boldsymbol{\epsilon}_n\,. \tag{61}$$

The time histories of the kinetic, internal and total energies presented in Figure 2 confirm, within machine precision, the conservation properties of the proposed algorithm in the case of a three-dimensional Noh test (Fig. 2(a)), and a three-dimensional Sedov test (Fig. 2(b)). The reader can refer to Section 8 for more details on the setup of these tests.

5. Variational multiscale stabilization

Variational multiscale stabilization of piece-wise linear discretizations of the Lagrangian hydrodynamics equations was already explored in [31, 33] for total Lagrangian formulations. The present article, instead, implements the approach proposed in [32], which directly applies the variational multiscale paradigm [15, 16, 18] to updated Lagrangian formulations. The variational multiscale analysis and design of the stabilization method are presented in complete detail in [32], and for the sake of brevity, are omitted here. Suffices to say that the multiscale analysis is based on a decomposition of the solution into a coarse-scale component, representable over the computational mesh, and a fine-scale component, which belongs to the subgrid space of unresolved scales. By finding appropriate approximations to the fine-scale solution, it is possible to stabilize the shock hydrodynamic equations from acoustic-type instabilities, responsible for the appearance of spurious hourglass modes in quadrilateral and hexahedral computations, and artificial stiffness in triangular and tetrahedral computations. As indicated in [32], a *minimalist* strategy (to obtain the simplest and most efficient expression for the stabilization terms) suggests to enrich the pressure and velocity with fine-scale components. Recalling the structure of the algorithmic stress (19) and

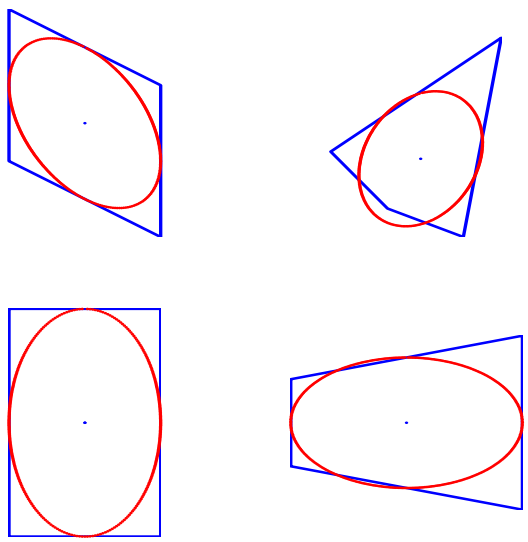

Figure 3: Sketch of the length-scale h_{art} as a function of the direction of $\boldsymbol{n}_{sh}$. The plots show the envelope of h_{art} as the angle that $\boldsymbol{n}_{sh}$ forms with the x_1-axis varies from 0 to 360 degrees. Note the smooth transition of the length-scale near the corners of the elements.

the algorithmic vector flux (20), we have:

$$\boldsymbol{\sigma}_{vms} = -p' \boldsymbol{I} \,, \tag{62}$$

$$\boldsymbol{\lambda}_{vms} = p^h \boldsymbol{v}' \,, \tag{63}$$

where p^h is the coarse-scale discrete pressure, p' is the fine-scale subgrid pressure, and $\boldsymbol{v}'$ is the fine-scale velocity. In particular, fine-scale pressure and velocity are approximated by residuals of a pressure and momentum equation, respectively. In the context of the proposed predictor/multi-corrector method, this amounts to set

$$p' = -\tau \left(\mathsf{Res}_p^h\right)_{n+1/2}^{(i)} \,, \tag{64}$$

$$\boldsymbol{v}' = -\tau \left(\rho \left.\frac{\partial \epsilon}{\partial p}\right|_{\rho} \frac{c_s^2}{p}\right)_{n+1/2}^{h;(i)} \left(\mathsf{Res}_v^h\right)_{n+1/2}^{(i,i+1)} \,, \tag{65}$$

$$\tag{66}$$

where c_s is the speed of sound in the medium, τ is the stabilization parameter with dimension of time, and

$$\left(\mathsf{Res}_p^h\right)_{n+1/2}^{(i)} = \frac{p_{n+1}^{h;(i)} - p_n^h}{\Delta t} + \left(\rho\, c_s^2\, \nabla_x \cdot \boldsymbol{v}\right)_{n+1/2}^{h;(i)} \,, \tag{67}$$

$$\left(\mathsf{Res}_v^h\right)_{n+1/2}^{(i,i+1)} = \rho_{n+1/2}^{h;(i)} \frac{\boldsymbol{v}_{n+1}^{h,(i+1)} - \boldsymbol{v}_n^h}{\Delta t} + \left(\nabla_x p\right)_{n+1/2}^{h;(i)} \,, \tag{68}$$

where $\boldsymbol{v}^h$ denotes the coarse-scale discrete velocity.

Remark9. Note that the term $\rho\, \partial_p \epsilon\big|_{\rho}$ is the inverse of the Grüneisen parameter, a quantity that is typically expressed as a pure function of the density ρ in Mie-Grüneisen constitutive models. The Grüneisen parameter varies very mildly away from phase transition states. This quantity and the speed of sound are usually provided by equations of state in tabular form.

Remark10. The term $\mathsf{Res}_p = \dot{p} + \rho\, c_s^2\, \nabla_x \cdot \boldsymbol{v}$ can be termed a pressure residual. It is indeed a residual since, as detailed in [32], the internal energy equation can be rearranged as $0 = \rho\, \partial_p \epsilon\big|_{\rho}\, \mathsf{Res}_p$. It was shown in [35] that the expression for Res_p can also be derived by considering isentropic processes in perfect materials (materials free from internal dissipation mechanisms), and that Res_p^h measures the *production* of entropy due to the numerical discretization. In regions of smooth flow, Res_p^h should vanish, but because of numerical instabilities, *numerical entropy* can be generated. It was also shown in [34, 35] that the same approximation can be obtained by linearizing the expression for $p' = p - p^h = \hat{p}(\rho, \epsilon) - p^h$ about p^h.

Remark11. With respect to the work in [35], the additional fine-scale velocity $\boldsymbol{v}'$ is used to stabilize the energy equation. $\boldsymbol{v}'$ is a scaled function of the momentum equation discrete residual. The specific scaling has the purpose of developing a stabilization operator which retains the structure of the Lagrangian hydrodynamics equations, represented by the system form of a nonlinear wave equation (see [32] for complete details). This is also the reason why the same scaling parameter τ (with dimension of time) is used for both fine-scale velocity and pressure.

Remark12. The term $\boldsymbol{\lambda}_{vms} = p^h \boldsymbol{v}'$ has the meaning of the work done by the interaction of the fine-scale velocity with the coarse-scale pressure.

Remark13. Observe that $\boldsymbol{\lambda}_{vms}$ is a function of the momentum equation residual, and, consequently, vanishes at pure contact discontinuities, where pressure and velocity are continuous and in particular constant. $\boldsymbol{\lambda}_{vms}$ has dimensions of a heat flux, but this interpretation would be erroneous, since heat fluxes are active at contact discontinuities.

Remark14. Also the fine-scale pressure p' vanishes at pure contacts, since the residual Res_p vanishes for constant velocity and pressure fields.

Remark15. It is easy to verify that the proposed stabilization approach satisfies Galilean invariance properties, since the velocity always appears in incremental form with respect to space or time. In [29–31], Galilean invariance properties were recognized as important for the specific case of Lagrangian and arbitrary Lagrangian-Eulerian (ALE) computations.

Remark16. When shock waves are present in the material, the analysis with which the proposed stabilization mechanism are derived does not apply. From a physical point of view, a shock wave is an infinitely thin layer in which the flow does not behave as a perfect material, due to internal dissipation mechanisms. At the numerical level, these irreversible mechanisms are introduced by shock-capturing operators in the form of artificial viscosities, which smear the discontinuity over a few cells of the computational grid.

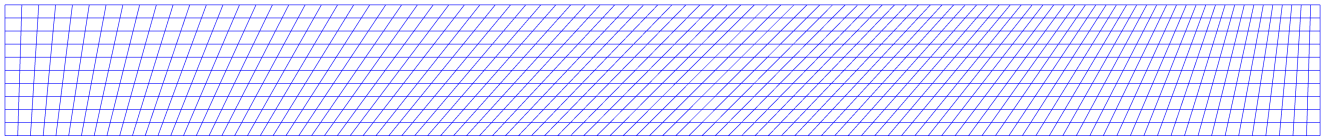

(a) Initial mesh.

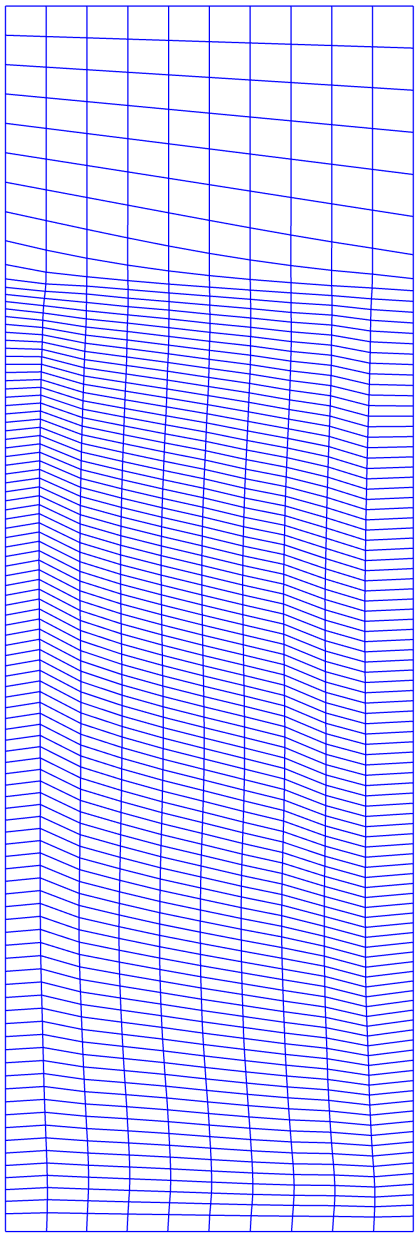

(b) VMS-P0 [34, 35].

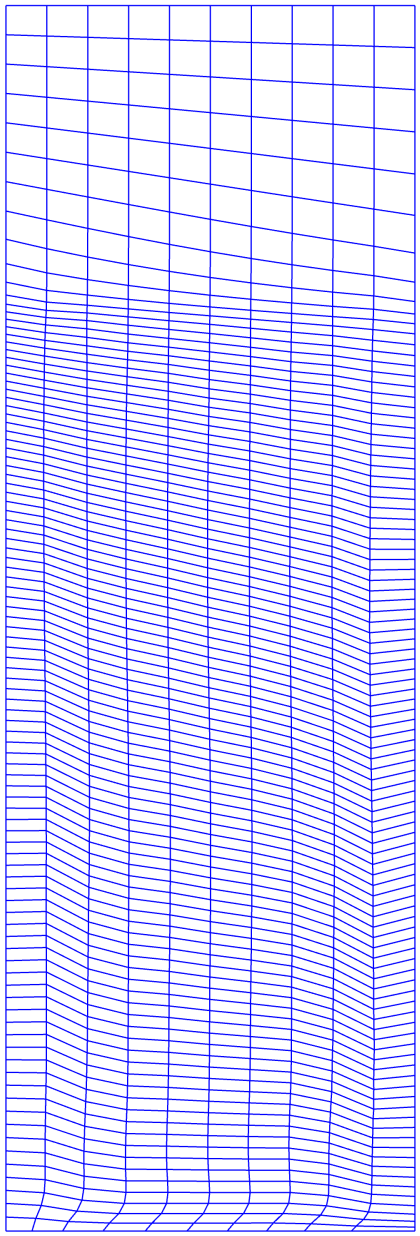

(c) VMS-C.

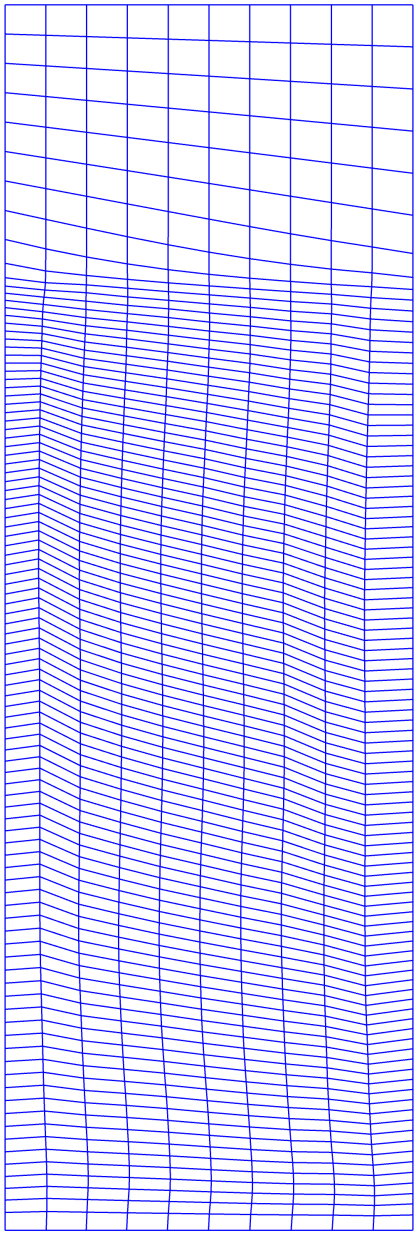

(d) VMS-AC [31, 33].

Figure 4: Saltzmann test. Comparison of the mesh displacement results for the VMS-P0, VMS-C, VMS-AC methods. The meshes in Figures 4(b), 4(c), 4(d) are rotated by 90 degrees counter-clockwise.

5.1. Choice of the stabilization parameters

The stabilization parameter τ is defined as in [32], using similar criteria to [31, 33, 35]:

$$\tau = c_\tau \frac{\Delta t}{2} \frac{CFL_{nominal}}{CFL_{actual}} \ . \tag{69}$$

where $CFL_{nominal}$ is the target global *Courant-Friedrichs-Levy* (CFL) number (specified by the user) while CFL_{actual} is the actual CFL number at time t. In practice the ratio $CFL_{nominal}/CFL_{actual}$ is almost always unity, so that $\tau = c_\tau \Delta t/2$, perfectly matching the definition given in [32]. The only exceptions are the startups of highly transients computations, in which time steps are initially forced to be very small and are progressively increased to nominal values by means of a compound (exponential growth) scaling. Under these conditions, the parameter τ, because of the scaling with Δt, would result extremely small, negatively affecting the spatial stability of the overall algorithm. After the initial transient has elapsed (typically involving between 30 and 50 time steps), the ratio $CFL_{nominal}/CFL_{actual}$ becomes and stays equal to unity. The value $c_\tau = 2$ (for which $\tau = \Delta t$) seemed to give the best results, although values in the range $[1/2, 3]$ proved also effective. Therefore, to a certain extent, the stability properties of the method are not overly sensitive to changes of the stabilization parameter value.

Remark17. The analysis of stability and accuracy presented in [36] shows that when three iterations of the predictor/multicorrector method are applied in combination with $c_\tau = 2$ and a safety parameter $CFL = 0.8$ (see also Section 7.1), very good performance is to be expected, since the method is characterized by high wave number dissipation, accurate low wave number behavior, and very low dispersion error over the entire wave number spectrum. These theoretical findings were confirmed in computations, not reported here, for the sake of brevity.

6. Artificial viscosity and discontinuity capturing operator

The discontinuity capturing operator is implemented as follows:

$$\boldsymbol{\sigma}_{art} = \begin{cases} \rho\, \nu_{art;v} \nabla_x^S \boldsymbol{v} \ , & \text{if } \nabla_x \cdot \boldsymbol{v} < 0 \ , \\ \boldsymbol{0}_{n_d \times n_d} \ , & \text{otherwise} \ . \end{cases} \tag{70}$$

$$\boldsymbol{\lambda}_{art} = \begin{cases} \rho\, \partial_p \epsilon\big|_\rho \ \nu_{art;p} \nabla_x p \ , & \text{if } \nabla_x \cdot \boldsymbol{v} < 0 \ , \\ \boldsymbol{0}_{n_d} \ , & \text{otherwise} \ . \end{cases} \tag{71}$$

The scaling and structure of $\boldsymbol{\lambda}_{art}$ are chosen with the purpose of dissipating pressure oscillations in the energy equation. The artificial viscosities are

$$\nu_{art;v} = c_1 |\nabla_x \cdot \boldsymbol{v}|\, h_{art}^2 \ , \tag{72}$$

$$\nu_{art;p} = c_2 \sqrt{\frac{|\nabla_x p|}{\rho}}\, h_{art}^{3/2} \ , \tag{73}$$

The values $c_1 = 1.4$ and $c_2 = 1.0$ were found to perform best in the computations of Section 8. Similarly to the case of the stabilization operator, there is some flexibility in choosing the viscosity constant, and other constant combinations were found to perform equally well.

Remark18. The values $c_1 = 1.4$ and $c_2 = 1.0$ were chosen so that $\nu_{art;v}$ and $\nu_{art;p}$ peak at about the same value in computations, while maintaining a slightly different spatial variation.

Remark19. Maybe the most striking peculiarity of the adopted discontinuity operator is the introduction of the diffusive term $\boldsymbol{\lambda}_{art}$ in the energy equation, in starch contrast, for example, with [35]. This idea was already incorporated in the method proposed in [33]. One would be tempted to think about $\boldsymbol{\lambda}_{art}$ as an artificial heat flux, but this interpretation would be incorrect. In fact, the term $\boldsymbol{\lambda}_{art}$ involves only pressure gradients, and not temperature (i.e., internal energy) gradients.

Remark20. Most importantly, the term $\boldsymbol{\lambda}_{art}$ is not active at contact discontinuities, where the pressure is continuous and typically constant. $\boldsymbol{\lambda}_{art}$ is only active where shocks are present, and because the corresponding artificial viscosity does not scale with the speed of sound, this term is expected to be fairly small in compression regions where the pressure gradients are small.

Remark21. The scaling of the viscosities is solely based on the gradient of the solution, since the variational multiscale stabilization is already designed to control acoustic (hourglass) instabilities.

Remark22. By construction, the integral term containing $\boldsymbol{\lambda}_{art}$ is compatible with a global conservation statement for the total energy. Note also that the pressure gradient is easily computable because the pressure field is approximated by piecewise linear (continuous) finite element shape functions (see also Section Section 4.1.5).

Remark23. The use of the symmetric gradient in the definition of $\boldsymbol{\sigma}_{art}$ ensures, at the continuum level, objectivity of the artificial viscosity operator [38]. The definition (70) is more effective in damping artificial pure shear motion, with respect to the more common definition [5]

$$\boldsymbol{\sigma}_{art} = -\left(\rho\, \nu_{art} \nabla_x \cdot \boldsymbol{v}\right) \boldsymbol{I} \ . \tag{74}$$

Artificially produced homogeneous shear motion can have disruptive consequences on shock hydrodynamics computations of fluids, since it is not resisted by hourglass controls (of any type), nor the discretized physical stress.

Remark24. The proposed artificial viscosity operators are Galilean invariant, because their expressions involve only gradients of velocity and pressure. Consequently, the proposed method is overall Galilean invariant.

The length-scale h_{art} is defined in a similar fashion to [33], and is designed to *stably* sample a mesh length along the normal to the shock front. This means that, for a given mesh, h_{art} should

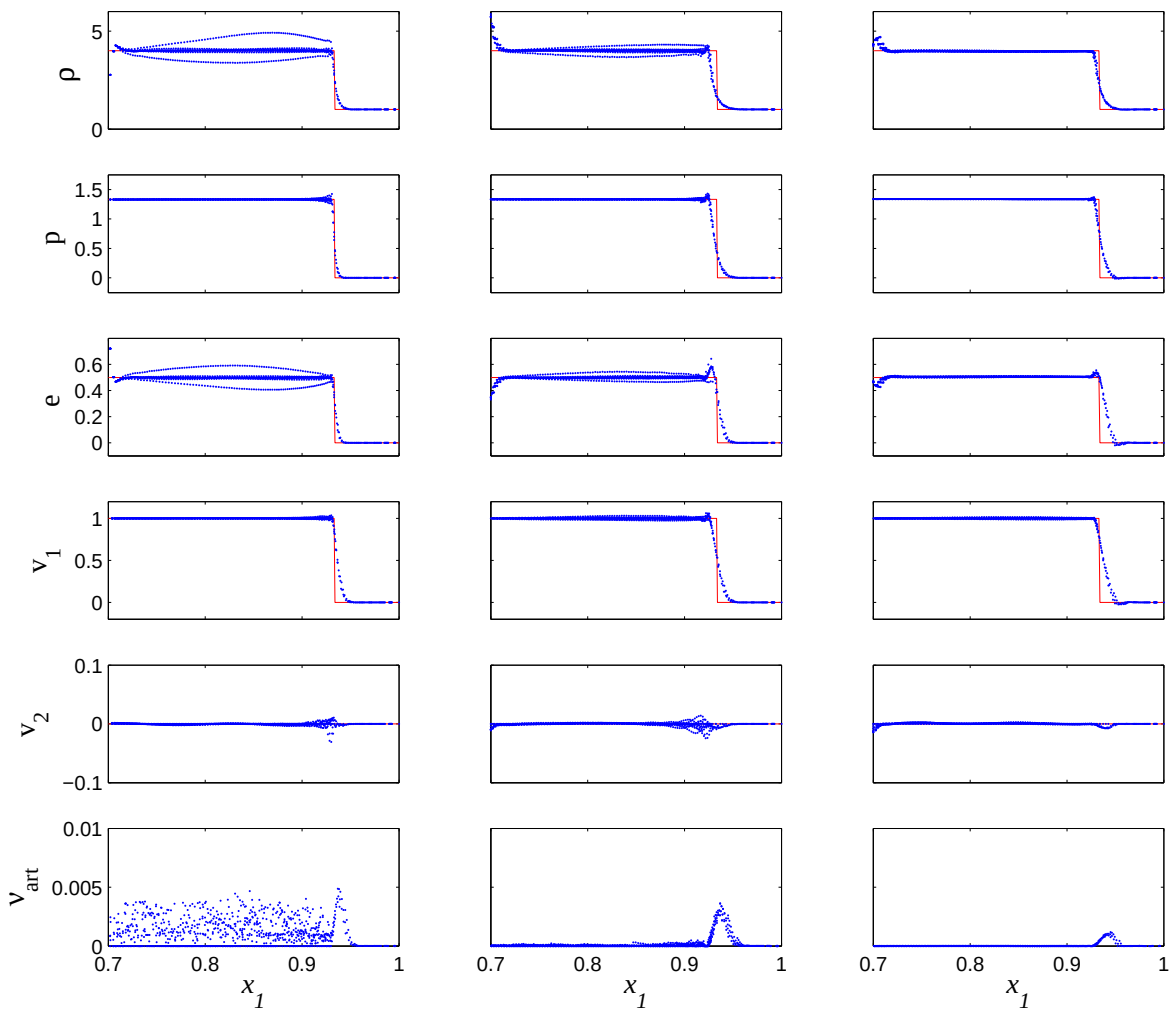

Figure 5: Saltzmann test, comparison against the exact solution (in red). Left column: VMS-P0 method. Center column: VMS-C method. Right column: VMS-AC method. From the top row down: Density, pressure, internal energy, horizontal velocity v_1, vertical velocity v_2, and artificial viscosities. The solution is plotted as a function of the coordinate x_1. The exact solution is represented by the continuous line, *the dots represent all the nodal values of the numerical solution* (projected along the x_2-coordinate onto a single plane).

not vary abruptly for small changes in the direction of the shock normal. An effective definition was found to be

$$h_{art} = \frac{2}{\sqrt{\boldsymbol{n}_{sh}^T \left(\boldsymbol{F}_\square \boldsymbol{F}_\square^T\right)^{-1} \boldsymbol{n}_{sh}}} \,, \tag{75}$$

$$\boldsymbol{F}_\square = \frac{\partial \boldsymbol{x}}{\partial \boldsymbol{\xi}} \,, \tag{76}$$

where $\boldsymbol{n}_{sh}$ is a unit vector in the direction normal to the shock front, and $\boldsymbol{F}_\square$ the gradient of the mapping from the element's parent domain to its current configuration. In practice, $\left(\boldsymbol{F}_\square \boldsymbol{F}_\square^T\right)$ measures the *stretch* in the direction given by $\boldsymbol{n}_{sh}$. A plot of the envelope of h_{art} as the shock normal angle spans the interval $[0, 360]$-degrees is presented in Figure 3, for various quadrilateral elements. This definition is analogous to the one adopted in [17]. A reliable approximation to $\boldsymbol{n}_{sh}$ was found to be:

$$\boldsymbol{n}_{sh} = \frac{0.75 \frac{\dot{\boldsymbol{v}}}{\|\dot{\boldsymbol{v}}\|} + 0.25 \frac{\nabla_x \rho}{\|\nabla_x \rho\|}}{\left\| 0.75 \frac{\dot{\boldsymbol{v}}}{\|\dot{\boldsymbol{v}}\|} + 0.25 \frac{\nabla_x \rho}{\|\nabla_x \rho\|} \right\|} \,. \tag{77}$$

Basically, the direction of the shock normal is a weighted average of the direction of the acceleration vector $\dot{\boldsymbol{v}}$, and the density gradient (see also [39, 40]). Again, there is some flexibility in the definition of the shock direction, and alternative choices are possible.

7. General considerations on implementation

7.1. CFL condition

The calculation of the Courant-Friedrichs-Levy (CFL) condition is based on the analysis in [36] of a linearized version

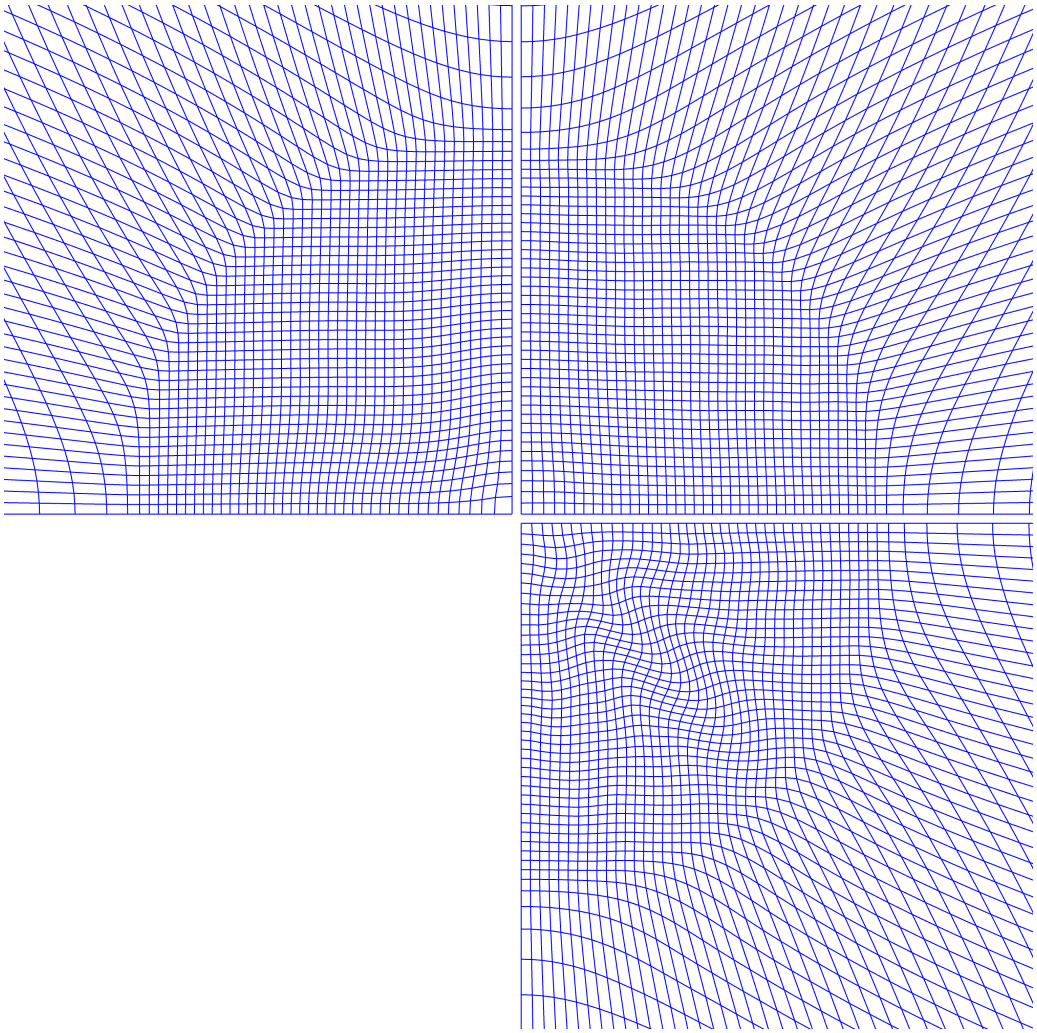

Figure 6: Two dimensional Noh test, mesh deformation. Comparison between the VMS-P0 method (upper left corner), the VMS-C method (upper right corner), and the VMS-AC method (lower right corner).

of the proposed algorithm in the case of one-dimensional periodic flows. This analysis precisely accounts for the effect of the parameter c_τ and the artificial viscosity on the overall stability, and yields the condition

$$\Delta t \leq CFL \min_{1\leq e\leq n_{el}} \left\{ \frac{h_e^2}{\nu_{art_e} + \sqrt{\nu_{art_e}^2 + c_\tau c_{s_e}^2 h_e^2}} \right\} . \tag{78}$$

The specific bound for the safety factor CFL depends on the number of iterations. In [36], it was found that for one and three iterations stability is achieved if $CFL < 1.0$, and for two and four iterations stability is achieved if $CFL < 0.9$.

Remark25. In the case when the artificial viscosity vanishes and $c_\tau = 1.0$, one recovers the classical condition

$$\Delta t \leq CFL \min_{1\leq e\leq n_{el}} \left\{ \frac{h_e}{c_{s_e}} \right\} . \tag{79}$$

Remark26. Conversely, in the case of a very low temperature fluid with artificial viscosity active, one recovers the CFL condition for the purely diffusive case, namely:

$$\Delta t \leq CFL \min_{1\leq e\leq n_{el}} \left\{ \frac{h_e^2}{2\nu_{art_e}} \right\} . \tag{80}$$

This situation is often encountered in hypervelocity impact or piston problems (i.e., the Saltzmann test in Section 8.1), in which the internal energy rises from a very low initial value as a result of kinetic energy conversion or work done on the system at its boundaries.

Unless otherwise stated, all computations presented in this article where run with three iterations of the predictor multi-corrector time integrator, $c_\tau = 2$, and $CFL = 0.8$, which corresponds to a very favorable condition in the linearized case, with high wave number dissipation, high accuracy in the low wave number range, and low dispersion error throughout the entire wave number spectrum (see [36] for a detailed justification of these claims).

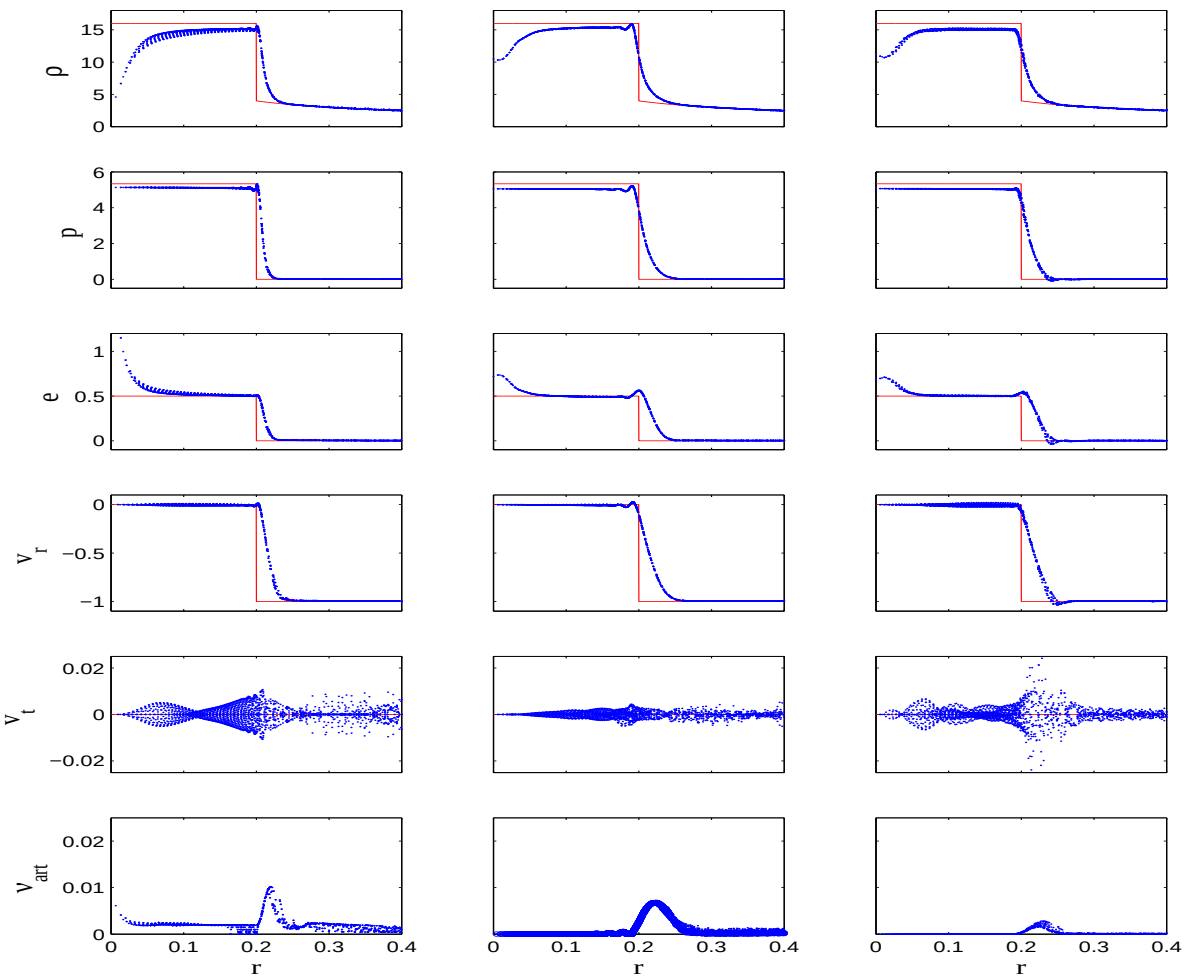

Figure 7: Two-dimensional Noh test on a Cartesian mesh: Comparison with the exact solution (in red). Left column: VMS-P0 method. Center column: VMS-C method. Right column: VMS-AC method. From the top row down: Density, pressure, internal energy, radial velocity v_r, tangential velocity v_t, and artificial viscosities. Each variable is plotted as a function of the radius $r = \sqrt{x_1^2 + x_2^2}$. All solution points are rotated around the origin to align on a single radial plane.

7.2. Notation

The quality, accuracy and robustness of the proposed method is evaluated by comparing it to two previously developed variational multiscale methods [33, 35], and other state of the art computations [1, 22]. In particular the following notation is used:

VMS-C indicates the *variational multiscale conservative* method, the newly proposed conservative approach to Lagrangian shock hydrodynamics.

VMS-AC indicates the *variational multiscale asymptotically conservative* method, proposed in [31, 33]. This method adopts an iterative predictor-corrector approach which is conservative only when convergence of the iterations is attained.

VMS-P0 indicates the *variational multiscale* $Q1/P0$ method, proposed in [34, 35]. This method is conservative, but maintains the typical structure of a standard hydrocode, in that all thermodynamic variables are approximated as piece-wise constant functions over the elements of the computational mesh.

8. Numerical computations

8.1. Saltzmann test

The Saltzmann test evaluates the ability of a numerical method to capture the features of a planar shock over a distorted mesh (see the initial mesh geometry in Fig. 4(a)). A rectangular domain of gas ($\gamma = 5/3, \rho_0 = 1$) is initially at rest, at zero temperature (i. e., for practical purposes, $\epsilon_0 = 10^{-14}$). At time t_0^+, the left boundary is set in motion with unit velocity, and generates a compression shock of infinite strength (infinite Mach number), propagating from left to right through the computational domain. All other boundary conditions are of "roller" type (zero normal velocity/displacement). Given a value of the

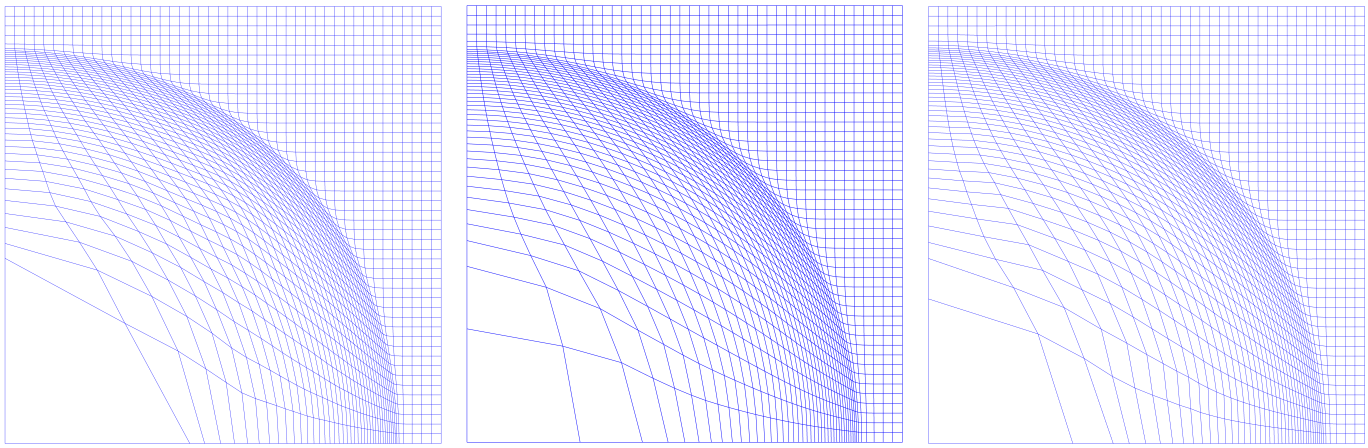

(a) VMS-P0 [34, 35]. (b) VMS-C. (c) VMS-AC [31, 33].

Figure 8: Two-dimensional Sedov test on a Cartesian mesh: Comparison of mesh deformation patterns.

ideal gas isentropic constant $\gamma = 5/3$, the thermodynamic state past the shock is given by values of pressure, internal energy, and density of $4/3$, $1/2$, 4, respectively. The Saltzmann test is both a robustness and an accuracy test. Computations are performed at $CFL = 0.8$, and compared at the final non-dimesional time $T = 0.7$.

Figures (Figs. 4(b), 4(c), 4(d)) show the mesh displacement results, where it can be observed that the mesh deformation pattern of VMS-C is somewhat intermediate between VMS-AC and VMS-P0. Similar conclusions are obtained by observing Figure 5, where the three methods (blue dots) are compared against the exact solution (red continuous line).

Remark27. The new conservative VMS-C method does not produce any negative undershoots, clearly manifest for the VMS-AC method. This is considered by the authors a considerable robustness improvement, especially for applications to more realistic materials for which equations of state are given in tabular rather than analytic form.

The VMS-AC method shows very good agreement with the *plateaus* of the exact solution for density and internal energy, while the VMS-P0 solution shows wide overshoots/undershoots near the lateral boundaries (the horizontal boundaries in Fig. 4(a)) of the computational domain. The VMS-C method has less pronounced overshoots near the horizontal boundaries, although the overshoot in the internal energy plot past the shock location is more pronounced than in both the VMS-P0 and VMS-AC results. Note that the VMS-P0 method utilizes a form of the artificial viscosity which also includes a term scaling with the speed of sound, while the artificial viscosities for the VMS-C and VMS-AC methods are purely based on the solution gradient: This is the reason for the different behavior of the artificial viscosity past the shock front, in the last row of plots in Figure 5.

Remark28. It is important to analyze the typical numerical challenges involved in the Saltzmann test. The numerical error in the shock region is responsible for a spurious component of the velocity, transverse to the shock front normal. At the horizontal boundaries, the roller boundary conditions force the transverse velocity to be zero, and are responsible for an increase in the kinetic energy error in the neighboring area. The numerical error on the kinetic energy is compensated by the numerical error in the internal energy, as the total energy is globally conserved (in a certain sense, "two wrongs make a right"), and the lumped mass matrix does not allow information to be redistributed globally over the mesh.

Remark29. In order to explain the behavior of the various methods under consideration, a number of additional tests, not reported here for the sake of brevity, showed the following trends: The combination of mass lumping and strict enforcement of conservation seems responsible for the over/undershoots near the boundary for the VMS-P0 and VMS-C methods. This phenomenon is somewhat expected as the lumping procedure, beneficial in the computation of shock discontinuities, effectively *localizes* the solution information. When lumping is used, the numerical forces and work associated to a particular degree-of-freedom cannot have their effect redistributed over neighboring nodes by the inversion of a diagonal lumped mass matrix, as opposed to the case of the consistent mass matrix.

Remark30. Instead, when the consistent mass matrix was used, the VMS-C method showed improved results near the horizontal boundaries, but produced negative undershoots of the internal energy ahead of the shock front. For this reason, this choice is not endorsed by the authors as viable.

8.2. Two-dimensional Noh test on a Cartesian quadrant

The Noh test [28] is an implosion test. The velocity has an initial uniform radial distribution (the velocity field points to the origin, and has unit magnitude, except at the origin, where it is forced to zero). The initial internal energy should be zero, but for practical purposes the value 10^{-14} is used. The gas constant $\gamma = 5/3$ is applied to all computations, and the initial density is set to a constant unit value. The shock speed is $1/3$, so that

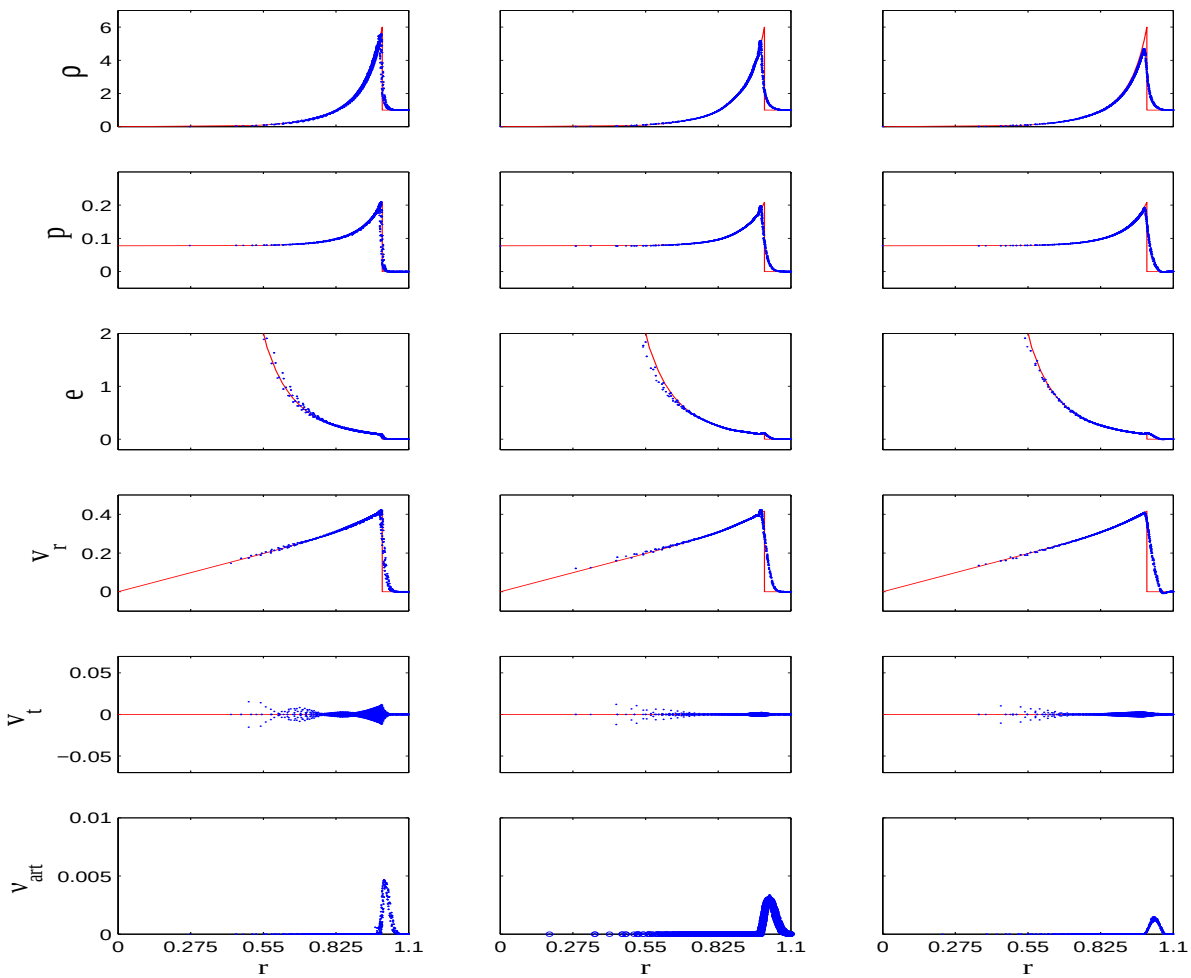

Figure 9: Two-dimensional Sedov test on a Cartesian mesh: Comparison with the exact solution (in red). Left column: VMS-P0 method. Center column: VMS-C method. Right column: VMS-AC method. From the top row down: Density, pressure, internal energy, radial velocity v_r, tangential velocity v_t, and artificial viscosities. Each variable is plotted as a function of the radius $r = \sqrt{x_1^2 + x_2^2}$. All solution points are rotated around the origin to align on a single radial plane.

at the final time of 0.6 in the computation, the discontinuity is found at $r = 0.2$. The exact solution for the density past the shock is 16.0 and decays as $1 + t/r$ in front of the shock, where t is time and $r = \sqrt{x_1^2 + x_2^2}$ is the radius. The values of pressure and internal energy past the shock are $16/3$ and $1/2$, respectively. The initial domain of a Cartesian quadrant $[0, 1] \times [0, 1]$ is subdivided into 50×50 squares.

The mesh deformation results presented in Figure 6 show that the best mesh deformation (in terms of regularity of the elements and smoothness of the mesh lines) is achieved with the VMS-C method. Overheating near the implosion corner produce element of larger area (i. e., lower density) in the case of the VMS-P0 method. The VMS-P0 and VMS-C methods show less mesh distortion because both use a similar definition of the element mesh length in the artificial viscosity, less prone to large variations in direction from element to element than the VMS-AC method. Figure 7 shows a comparison against the exact solution. The density and internal energy plots for the VMS-P0 method are affected by a pronounced overheating error near the origin (for a full description of numerical overheating errors, see [28]). These errors are much reduced in the case of the VMS-AC and VMS-C methods, due to the specific form of the discontinuity capturing operator adopted. Again, the thermodynamic variables computed with the VMS-C method are all positive, while the VMS-AC method produces negative undershoots in internal energy and pressure. With respect to the VMS-P0 solution, the VMS-C solution presents an internal energy overshoot past the shock, but has lower transverse velocity error. In general, the numerical solutions computed with the three methods are in good agreement with the exact solution, considering the coarseness of the mesh (for extensive studies on this problem, see, e.g., [28]). In the case of the density plot, the VMS-P0 method presents a more pronounced angular dispersion of the numerical data with respect to the VMS-C method, also confirmed in the tangential velocity plots.

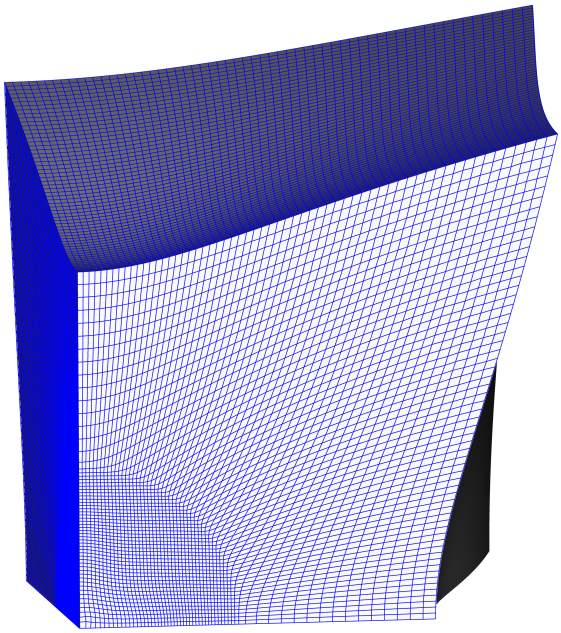

(a) VMS-P0 method.

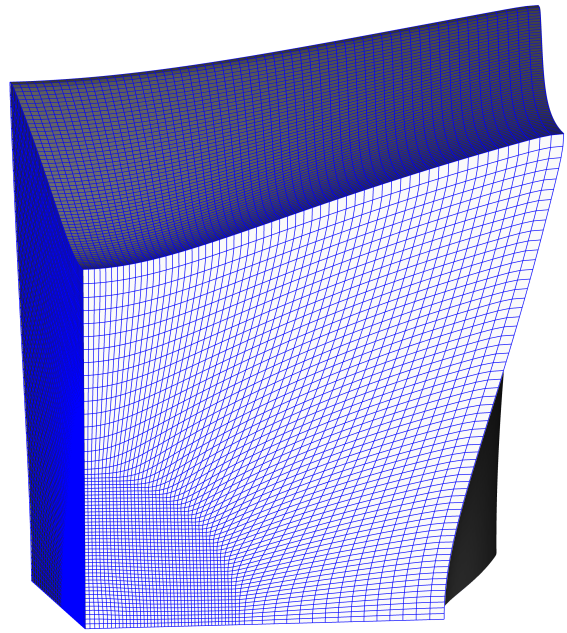

(b) VMS-C method

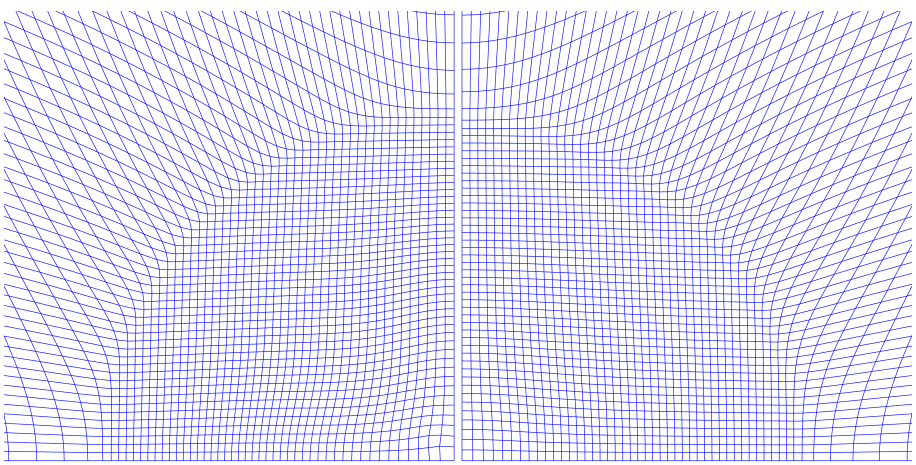

(c) Zoomed view. Left: VMS-P0 method. Right: VMS-C method,

Figure 10: Three-dimensional Noh test on a Cartesian mesh: Mesh deformation for the test performed on the 60^3 mesh.

In general the VMS-P0 method yields sharper shock profiles than the VMS-C method, at the expense of higher transverse/tangential velocity errors, and a more pronounced dispersion of the data around the exact, symmetric solution.

8.3. Two-dimensional Sedov test on a Cartesian quadrant

The Sedov test is a multi-dimensional blast test. An exact solution, which possesses cylindrical symmetry, is derived with self-similarity arguments in [37].

The proposed version of the Sedov blast test is performed on the $[0, 1.1]\times[0, 1.1]$ quadrant, subdivided into 45^2 initially identical squares, and assesses the ability of the method to respect the cylindrical symmetry. The initial density has a uniform unit distribution, $\gamma = 1.4$, and the internal energy is "zero" (actually, 10^{-14}) everywhere, except the first square zone on the bottom left corner of the quadrant, near the origin, where it takes the value, $0.9792/(4h^2) = 409.7$, with $h = 1.1/45$ the initial length of the side of the mesh quadrilaterals [37].

In the case of the VMS-C and VMS-AC methods, the internal energy initial condition is further projected onto the nodal finite element basis used to approximate the thermodynamic variables [33]. The mesh deformation results are shown in Figure 8. Since the exact solution is obtained by self-similarity arguments and has radial symmetry, the mesh deformation is expected to be smooth. Figure 8(b) shows a clear superiority for the VMS-C method, in terms of mesh displacements (similar deformation patterns, although more distorted, can be observed for the VMS-AC method in Fig. 8(c)). On the other hand, the results for the VMS-P0 method show a pronounced distortion in the element near the origin, possibly due to the onset of an hourglass mode, as already observed in [34, 35].

A comparison of the three approaches with respect to the ex-

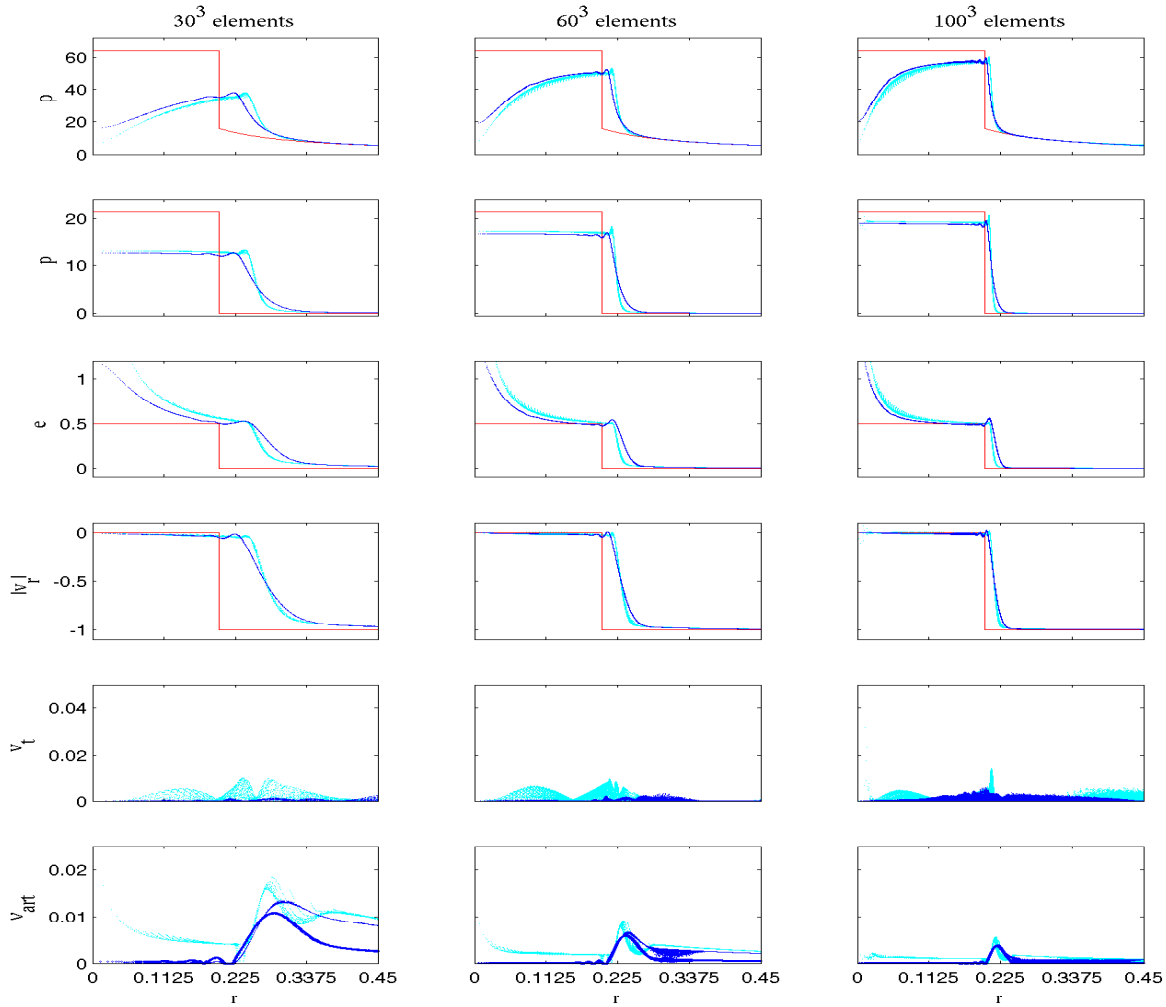

Figure 11: Three-dimensional Noh test on a Cartesian mesh: Comparison with the exact solution (in red) for the 30^3 (left), 60^3 (center), and 100^3 (right) meshes. In light blue (cyan), the VMS-P0 method, in dark blue the VMS-C method. From the top row down: Density, pressure, internal energy, radial velocity v_r, tangential velocity v_t, and artificial viscosities. Each variable is plotted as a function of the radius $r = \sqrt{x_1^2 + x_2^2}$. All solution points are rotated around the origin to align on a single radial plane.

act solution is presented in Figure 9. Considering the density plots, the results indicate that the VMS-P0 method is the closest to the exact solution, followed (in terms of accuracy), by the VMS-C and VMS-AC methods. Specifically, the density peak, a good indicator of the overall quality of the computation, is at 5.35 for the VMS-C method, against 5.58 for the VMS-P0 method and only 4.84 for the VMS-AC method. The results of Figure 8 for the mesh displacements are also confirmed by the tangential velocity plots, which show that the VMS-C method has the smallest tangential velocity error.

Remark31. As shown in in Figure 9, the values of the artificial viscosity are lower for the VMS-C and VMS-AC methods with respect to the VMS-P0 method. This resulted in a reduction in the number of time steps to complete the computation on the order of 30%. It is important to notice the higher accuracy that the VMS-C method shows in capturing the solution with respect to the VMS-AC method. The different choice of artificial viscosity and stabilization are responsible for the improvement in the results.

8.4. Three-dimensional Noh test on a Cartesian octant

The initial conditions for the Noh test in three dimensions are identical to the two-dimensional case, but will generate a more intense, spherical shock pattern. In this case, since the shock Mach number is infinite for both the two- and three-dimensional case, the density ratio is a better indicator of the shock intensity. In the three-dimensional case, this ratio is 64, against 16 for the two-dimensional case. The domain $[0, 1.1] \times [0, 1.1] \times [0, 1.1]$ is uniformly meshed with three meshes of resolution $30^3 = 27,000$, $60^3 = 216,000$, and $100^3 = 1,000,000$ cubes. A radial shock propagates with speed $1/3$ in the computational domain, so that at the final time of 0.6 in the computation, the discontinuity is found at $r = 0.2$. The exact solution for the density behind the shock is 64.0 and decays as $(1 + t/r)^2$ in front of the

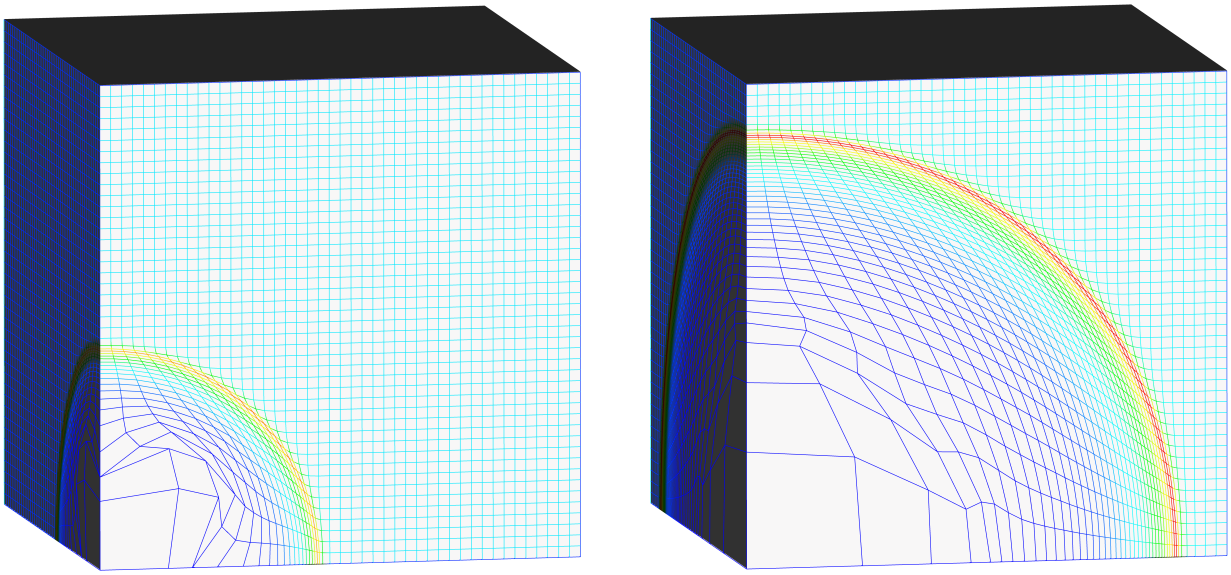

(a) VMS-P0 method. (b) VMS-C method.

Figure 12: Three-dimensional Sedov test on a Cartesian mesh of 44^3 elements: The VMS-P0 method, could not be run to completion (Fig. 12(a)), due to an hourglass pattern developing near the coordinate origin. The VMS-C method (Fig. 12(b)) did not experience the onset of hourglass modes, and could be run successfully.

shock, where t is time and $r = \sqrt{x_1^2 + x_2^2 + x_3^2}$ is the radius. Past the shock, the pressure and internal energy take the values $64/3$ and $1/2$, respectively.

Similarly to what was already observed in the two-dimensional setting, also the three-dimensional results show larger distortion in the mesh near the coordinate origin for the VMS-P0 method (Fig. 10(a)), than the VMS-C method (Fig. 10(b)). Again, this is a consequence of larger overheating errors for the VMS-P0 with respect to the VMS-C method, as appreciable in the comparison with the exact solution presented in Figure 11. Because the VMS-AC method was never implemented in three dimensions, we do not present any comparisons with such approach. We would expect, however, a trend very similar to the two-dimensional case.

As in the two-dimensional case, the VMS-P0 method shows somewhat sharper shock profiles than the VMS-C method, at the expense of a more pronounced overshoot in the pressure, a larger internal energy overheating, a larger scattering of the data about the exact solution, and, particularly, larger errors in the tangential velocity. Both solutions converge to the exact solution as the mesh is refined, and the overall numerical errors are within the bounds of what is expected for these mesh resolutions [28].

8.5. Three-dimensional Sedov test on a Cartesian octant

The proposed version of the Sedov blast test is performed on the $[0, 1.1] \times [0, 1.1] \times [0, 1.1]$ octant, subdivided into $22^3 = 10,648$, $44^3 = 85,184$, $88^3 = 681,472$ cubic elements. This refinement study is aimed at evaluating the robustness of the method, since, as the mesh-spacing is refined, the initial internal energy distribution is changed so that all the initial internal energy keeps being concentrated in the element adjacent to the coordinate origin. This amounts to setting the initial distribution of internal energy to zero, with the exception of the nearest element to the origin for which $\epsilon_0 = 0.851/(8h^3)$, with h the initial length of the sides of the cubic elements [37]. Note also that because the initial conditions are changed as the mesh is refined, this particular setup of the refinement study cannot be used to evaluate convergence rates. As in the two-dimensional case, the initial conditions for the thermodynamic variables were projected onto the nodal basis.

Remark32. The Sedov test in three dimensions is much more challenging than its two-dimensional counterpart, as it can more easily trigger hourglass-type instabilities, for two fundamental reasons: On the one hand, the spherical pattern of the flow is responsible for a higher concentration of internal energy; on the other hand, the space of hourglass modes is much larger in three than in two dimensions. In fact, while there are 2 hourglass modes out of 8 kinematic modes for a two-dimensional quadrilateral, there are actually 12 hourglass modes out of 24 kinematic modes for a three dimensional hexahedron [3]. Since a Cartesian mesh is used to represent a spherical flow, it is guaranteed that all the hourglass modes are to some extent excited.

The most remarkable result is that the VMS-P0 method *does not* pass the refinement test. Using the implementation detailed in [34], it was only possible to run successfully the case on the 22^3 mesh. Already in the case of the 44^3 mesh, due to a spurious hourglass pattern, two nodes of the mesh *collpased* to infinitesimal distance, driving the time step to zero, as evident in Figure 12(a). This, in spite of the fact that, in contrast to the two-dimensional case, even for the VMS-P0 method the initial condition on the internal energy was smoothed by first performing a nodal projection, and then re-averaging the re-

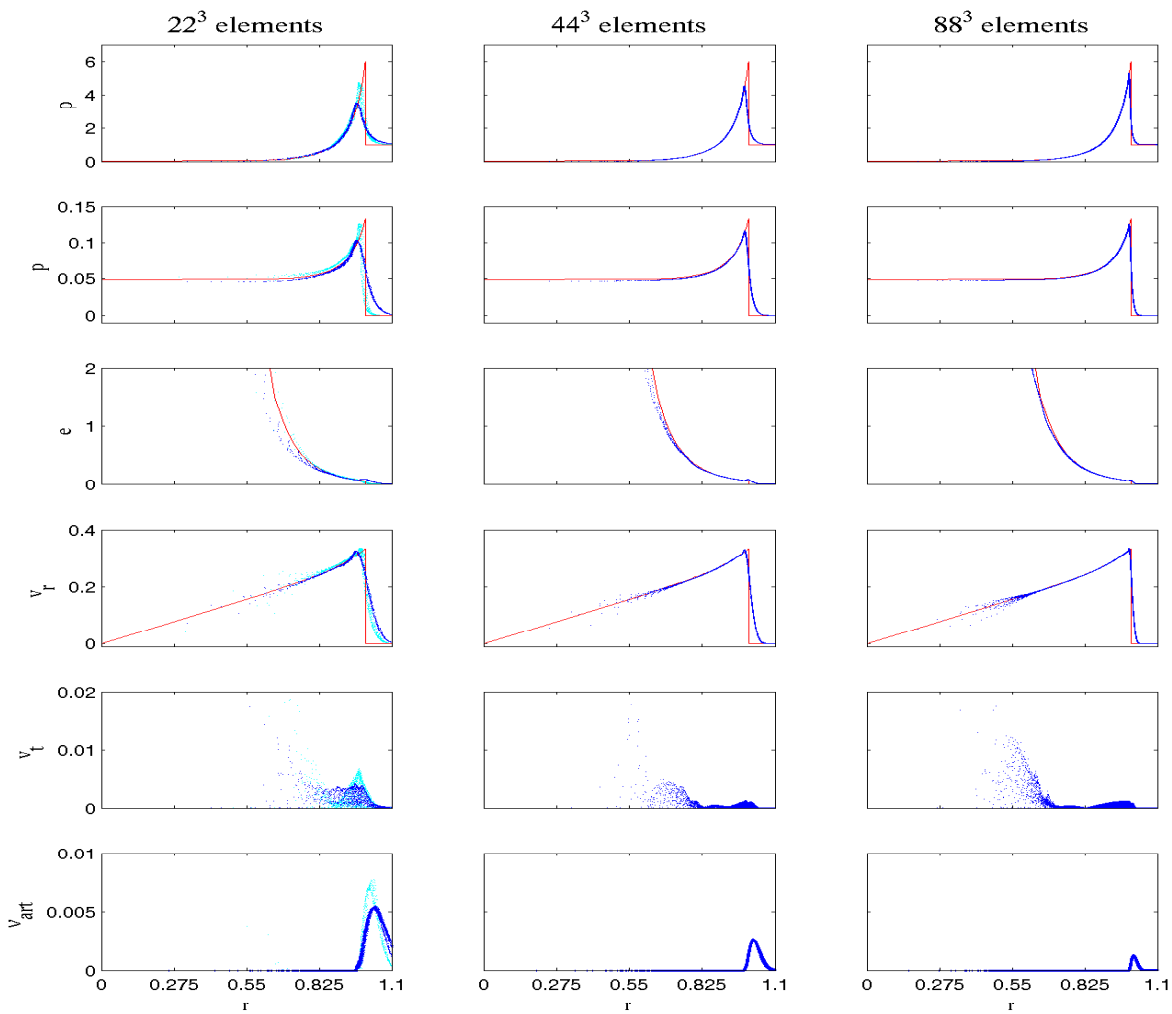

Figure 13: Three-dimensional Sedov test on a Cartesian mesh: Comparison with the exact solution (in red) of computations performed on a 22^3 mesh (left column), 44^3 mesh (center column), and 88^3 mesh (right column). In light blue (only on the left column) the VMS-P0 method, in dark blue the VMS-C method. On the left column, from the top down: Pressure, density and internal energy. On the right column, from top down: Radial velocity v_r, tangential velocity v_t, and artificial viscosities. Each variable is plotted as a function of the radius $r = \sqrt{x_1^2 + x_2^2 + x_3^2}$.

sult on each of the elements of the initial mesh (see [34]). In this particular test, the VMS-P0 method performance should be taken as indicative of a typical finite element or finite difference method for shock hydrodynamics based on piece-wise constant thermodynamic variables and shock capturing artificial viscosities. In fact, we also replaced the variational multiscale hourglass control in the VMS-P0 method with a Flanagan-Belytschko viscous hourglass control [13], and found no substantial improvement on the results. More specifically, the large values of the Flanagan-Belytschko hourglass viscosity needed to run the 22^3-element test case precluded robust computations in the case of the three-dimensional Noh test (see, for more details, [34]). This is by no means a critique of the Flanagan-Belytschko hourglass control [13], originally designed to stabilize solid mechanics computations, and very effective in this context. It is unclear if stabilization methods such as subzonal masses/pressures [9] are a viable choice for this challenging problem, as the presented three-dimensional test on Cartesian geometry has not been reported in the literature.

On the contrary, Figure 12(b) shows how easily the VMS-C method passes the test. The slight distortion in the mesh is due to a small acoustic pulse produced by the artificial viscosity in the initial stages of the transient, and should not be mistaken for an hourglass pattern: Extensive testing and analysis of the dynamic transient confirms this claim.

Figure 13 shows a comparison of the VMS-P0 and VMS-C methods with the exact solution. We observe that the thermodynamic variables are converging to the exact solution for the VMS-C method, while the error in the transverse velocity does not seem to converge in the L^∞-norm (the maximum norm). This is thought to depend on the increased intensity of the spurious acoustic pulse as the mesh is refined (due to the increased localization of initial internal energy near the origin). Observe that, as the mesh is refined, the region of convergence of the ra-

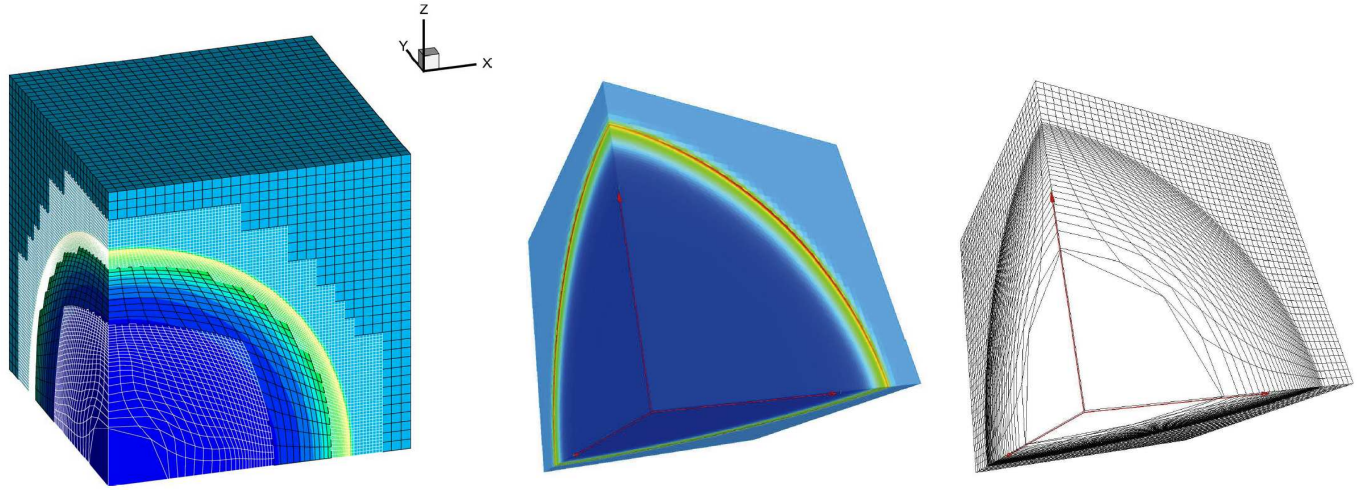

(a) Computations in [1].

(b) Computations in [22]. Right: density contours. Left: mesh deformation.

Figure 14: Three-dimensional Sedov test on a Cartesian mesh, results from the computations performed in [1] (Fig. 14(a)), and in [22] (Fig. 14(b)). Contour plot of the density and mesh deformation outline.

dial velocity extends further and further from the shock towards the origin, meaning that there is convergence in a point-wise and L^1-/L^2-integral sense.

One important point of note is the fact that the proposed VMS-C method shows very low radial dispersion of the data (particularly, pressure and density). This may be due to the fact that the mesh distortion near the origin is very moderate in computations (compare also with Figs. 14(a) and 14(b)). In summary, from the presented results, it is clear that the VMS-C method shows exceptional robustness with respect to the VMS-P0 method.

The only sources in the literature in which the proposed three-dimensional Sedov test was attempted are found in the work of Anderson *et al.* [1], in which adaptive multi-resolution (AMR) techniques in combination with a traditional finite volume/finite difference method are used, and in the very promising work of Nkonga and Maire [22], where successful computations on 20^3- and 40^3-element meshes are performed, using a Godunov-type finite volume method. These results are summarized in Figures 14 and 15, to help the reader in the comparisons.

Although the absence of quantitative results in [1] makes it difficult to precisely compare results, a few observations can be made. In the opinion of the authors, the AMR refinement/derefinement procedure applied in the computations in [1] may have a beneficial effect in filtering out hourglass modes. These effects are however difficult to reliably control, as the AMR technique is not targeted at removing hourglass *per se*. The density contour/mesh deformation plot of Figure 14(a) shows still a considerable amount of distortion in the element near the coordinate origin, due to the onset of an hourglass mode (for more details on this interpretation, see [34, 35]).

A similar distortion pattern is also seen in the case of the results in Figure 14(b) using the method in [22], which did not however prevent the computations from running to completion on 20^3- and 40^3-element meshes. Considering the density contours in Figure 14(b), the effect of the mesh distortion may be responsible for a larger dispersion of the data (especially near the density peak) in Figure 15. Analyzing more carefully the color scheme in Figure 14(b) (relative to the 40^3-cell grid), it is possible to observe that the darker red color (representing higher density values) is found in the center of the computational domain, away from the edges aligned with the Cartesian axes. This seems to indicate that the density peaks at the interior of the computational domain, away from edge boundaries. In the case of the VMS-C method in Figure 12(b), instead, this pattern does not appear, and the iso-surfaces at constant density stay very close to spherical. The results in Figure 15 compare otherwise well with the VMS-C method. Considering Figure 15 and the 20-element computation, most of the data points cluster at the peak value of 4, and some reach the higher value of 4.8: these results compare well with the 22^3-element computations performed with the VMS-C method in Figure 13. In particular, the VMS-C method yields a lower peak of the density, probably due to the fact that at this resolution level, the mentioned nodal projection of the initial condition may reduce the peak value of the initial internal energy pulse. For finer meshes, instead, the density peak produced by the VMS-C method at the final instant of the computation becomes considerably sharper. Returning to Figure 15, in the 40-element computation, most of the data points cluster at the peak value 5, and some reach the value 5.5, in good comparison with the results for the VMS-C method on the 44^3-element mesh in Figure 13. No results on meshes of fineness comparable with the 88^3-element case of Figure 13 are presented in [22].

9. Summary

This work documents the developments of an updated Lagrangian stabilized formulation for Lagrangian shock hydrodynamics for materials obeying a generalized caloric or Mie-Grüneisen equation of state. A complete presentation of the

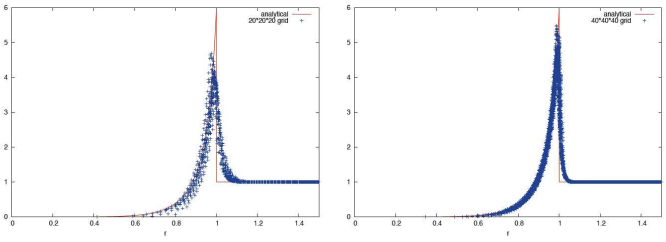

Figure 15: Three-dimensional Sedov test on a Cartesian mesh, results from the computations performed in [22]. The density is plotted for a resolution of 20^3 elements (left) and 40^3 elements. The density is plotted as a function of the radius $r = \sqrt{x_1^2 + x_2^2 + x_3^2}$, and all the data is collapsed on a single radial plot.

variational multiscale general methodology used to derive the method proposed here can be found in [32], in which stability properties are thoroughly discussed. The proposed algorithm derives from and combines recent work of the authors in the context of stabilization of Lagrangian hydrodynamics systems [31, 33] and strictly conservative time integration techniques [34, 35]. The reader can also refer to [36], in which a von Neumann stability analysis of the method is performed for the specific time integrator adopted in the numerical computations.

Extensive numerical computations on quadrilateral and hexahedral elements in two and three dimensions have been presented and compared with results from previous developments by some the authors and with state-of-the-practice computations by other research groups. In particular, a number of three-dimensional Sedov test computations showed encouraging results in terms of the robustness of the method with respect to instabilities of hourglass type, which can be considered as virtually absent. Additional work should be devoted to thoroughly testing the present methodology in the case of triangular and tetrahedral meshes in two and three dimensions, and comparing the results to the ones produced in [33].

Acknowledgments

The authors would like to acknowledge and thank for very valuable discussions Dr. M. Shashkov at Los Alamos National Laboratory, Dr. W. Rider, Dr. A. Robinson, and Dr. P. Bochev at Sandia National Laboratories, Dr. B. Déspres and Dr. B. Rebourcet at Commissariat à l'Energie Atomique (CEA, France), Dr. P.-H. Maire at UMR-CELIA-CEA-University of Bordeaux, Dr. M. Ricchiuto at INRIA-Bordeaux, Prof. R. Abgrall at the University of Bordeaux, and Dr. Santiago Badia, at Universitat Politècnica de Catalunya (Barcelona). The first and third authors would also like to thank Dr. R. Summers and Dr. S. Collis, at Sandia National Laboratories, for support and encouragement during the development of this research work.

References

[1] R. W. Anderson, N. S. Elliott, and R. B. Pember. An arbitrary Lagrangian-Eulerian method with adaptive mesh refinement for the solution of the Euler equations. *Journal of Computational Physics*, **199**(2):598–617, 2004.

[2] A. Barlow. A compatible finite element multi-material ALE hydrodynamics algorithm. *International Journal for Numerical Methods in Fluids*, **56**(8):953–964, 2008.

[3] T. Belytschko, W. K. Liu, and B. Moran. *Nonlinear Finite Elements for Continua and Structures*. J. Wiley & Sons, New York, 2000.

[4] D. J. Benson. A new two-dimensional flux-limited shock viscosity for impact calculations. *Computer Methods in Applied Mechanics and Engineering*, **93**:39–95, 1991.

[5] D. J. Benson. Computational methods in Lagrangian and Eulerian hydrocodes. *Computer Methods in Applied Mechanics and Engineering*, **99**:235–394, 1992.

[6] J. C. Campbell and M. J. Shashkov. A compatible Lagrangian algorithm for unstructured grids. Technical report, LA-UR-00-3231, Los Alamos National Laboratory, 2000.

[7] J. C. Campbell and M. J. Shashkov. A tensor artificial viscosity using a mimetic finite difference algorithm. Technical report, LA-UR-00-2290, Los Alamos National Laboratory, 2000.

[8] J. C. Campbell and M. J. Shashkov. A tensor artificial viscosity using a mimetic finite difference algorithm. *Journal of Computational Physics*, **172**:739–765, 2001.

[9] E. J. Caramana and M. J. Shashkov. Elimination of artificial grid distortion and hourglass-type motions by means of Lagrangian subzonal masses and pressures. *Journal of Computational Physics*, **142**(2):521–561, 1998.

[10] E. J. Caramana, M. J. Shashkov, and P. P. Whalen. Formulations of artificial viscosity for multi-dimensional shock wave computations. *Journal of Computational Physics*, **144**:70–97, 1998.

[11] B. Després and C. Mazeran. Symmetrization of Lagrangian gas dynamic in dimension two and multidimensional solvers. *Comptes Rendus Mecanique*, 331(7):475–480, 2003.

[12] B. Després and C. Mazeran. Lagrangian gas dynamics in two dimensions and Lagrangian systems. *Archives of Rational Mechanics and Analysis*, 178(3):327–372, 2005.

[13] D. P. Flanagan and T. Belytschko. A uniform strain hexahedron and quadrilateral with orthogonal hourglass control. *International Journal for Numerical Methods in Engineering*, **17**(5):679–706, 1981.

[14] T. J. R. Hughes. *The Finite Element Method: Linear Static and Dynamic Finite Element Analysis*. Prentice-Hall, Englewood Cliffs, New Jersey, 1987. (Dover reprint, 2000).

[15] T. J. R. Hughes. Multiscale phenomena: Green's functions, the Dirichlet-to-Neumann formulation, subgrid-scale models, bubbles and the origin of stabilized methods. *Computer Methods in Applied Mechanics and Engineering*, **127**:387–401, 1995.

[16] T. J. R. Hughes, G.R. Feijóo, L. Mazzei, and J.-B. Quincy. The Variational Multiscale Method — a paradigm for computational mechanics. *Computer Methods in Applied Mechanics and Engineering*, **166**:3–24, 1998.

[17] T. J. R. Hughes, M. Mallet, and A. Mizukami. A new finite element formulation for computational fluid dynamics: II. Beyond SUPG. *Computer Methods in Applied Mechanics and Engineering*, **54**:341–355, 1986.

[18] T. J. R. Hughes, G. Scovazzi, and Franca L.P. Multiscale and stabilized methods. In E. Stein, R. de Borst, and T. J. R. Hughes, editors, *Encyclopedia of Computational Mechanics*. John Wiley & Sons, 2004.

[19] E. Love and G. Scovazzi. On the angular momentum conservation and incremental objectivity properties of a predictor/multi-corrector method for Lagrangian shock hydrodynamics. Computer Methods in Applied Mechanics and Engineering, 2009. Submitted.

[20] P.-H. Maire. A high-order cell-centered Lagrangian scheme for two-dimensional compressible fluid flows on unstructured meshes. accepted, J. Comput. Phys., doi:10.1016/j.jcp.2008.12.007, 2009.

[21] P.-H. Maire and J. Breil. A second-order cell-centered Lagrangian scheme for two-dimensional compressible flow problems. *International Journal for Numerical Methods in Fluids*, **56**:1417–1423, 2008.

[22] P.-H. Maire and B. Nkonga. Multi-scale Godunov-type method for cell-centered discrete Lagrangian hydrodynamics. to be pusblished in J. Comput. Phys. and available at http://hal.inria.fr/inria-00290717/fr/, 2008.

[23] L. G. Margolin. A centered artificial viscosity for cells with large aspect ratios. Technical report, UCRL-53882, Lawrence Livermore National Laboratory, 1988.

[24] L. G. Margolin and M. Shashkov. Second-order sign-preserving conservative interpolation (remapping) on general grids. *Journal of Computational Physics*, 184(1):266–298, 2003.

[25] L. G. Margolin and M. Shashkov. Remapping, recovery and repair on a staggered grid. *Computer Methods in Applied Mechanics and Engineering*, 193(39-41):4139–4155, 2004.

[26] L. G. Margolin and M. Shashkov. Finite volume methods and the equations of finite scale: A mimetic approach. *International Journal for Numerical Methods in Fluids*, 56(8):991–1002, 2008.

[27] R. Menikoff and B. J. Plohr. The Riemann problem for fluid flow of real materials. *Reviews of Modern Physics*, **61**(1):75–130, 1989.

[28] W. F. Noh. Errors for calculations of strong shocks using an artificial viscosity and an artificial heat flux. *Journal of Computational Physics*, **72**:78–120, 1987.

[29] G. Scovazzi. A discourse on Galilean invariance and SUPG-type stabilization. *Computer Methods in Applied Mechanics and Engineering*, **196**(4–6):1108–1132, 2007.

[30] G. Scovazzi. Galilean invariance and stabilized methods for compressible flows. *International Journal for Numerical Methods in Fluids*, **54**(6–8):757–778, 2007.

[31] G. Scovazzi. Stabilized shock hydrodynamics: II. Design and physical interpretation of the SUPG operator for Lagrangian computations. *Computer Methods in Applied Mechanics and Engineering*, **196**(4–6):966–978, 2007.

[32] G. Scovazzi. Stabilized shock hydrodynamics: III. A new stabilization concept for Lagrangian Computations. Computer Methods in Applied Mechanics and Engineering, 2009. Submitted.

[33] G. Scovazzi, M. A. Christon, T. J. R. Hughes, and J. N. Shadid. Stabilized shock hydrodynamics: I. A Lagrangian method. *Computer Methods in Applied Mechanics and Engineering*, **196**(4–6):923–966, 2007.

[34] G. Scovazzi, E. Love, and M. J. Shashkov. A multi-scale Q1/P0 approach to Lagrangian shock hydrodynamics. Technical report, SAND2007-1423, Sandia National Laboratories, New Mexico, March 2007. Available at: `http://www.cs.sandia.gov/~gscovaz`.

[35] G. Scovazzi, E. Love, and M. J. Shashkov. A multi-scale Q1/P0 approach to Lagrangian shock hydrodynamics. *Computer Methods in Applied Mechanics and Engineering*, **197**(9–12):1056–1079, 2008.

[36] G. Scovazzi, W. J. Rider, E. Love, and J. N. Shadid. Stabilized shock hydrodynamics: V. Von Neumann stability analysis of a predictor/multi-corrector Lagrangian method. Computer Methods in Applied Mechanics and Engineering, 2009. Submitted.

[37] L. I. Sedov. *Similarity and Dimensional Methods in Mechanics*. Academic Press, New York, 1959.

[38] J. C. Simo and T. J. R. Hughes. *Computational Inelasticity*. Springer, New York, 1998.

[39] T. E. Tezduyar and M. Senga. Stabilization and shock-capturing parameters in SUPG formulation of compressible flows. *Computer Methods in Applied Mechanics and Engineering*, **104**:397–422, 1993.

[40] T. E. Tezduyar, M. Senga, and D. Vicker. Computation of inviscid supersonic flows around cylinders and spheres with the SUPG formulation and YZβ shock-capturing. *Computational Mechanics*, **38**:469–481, 2006.